Summer 2012

Operation of the aerodynamic plasma actuator at high altitude

Timothy Glen Nichols

Recommended Citation

Nichols, Timothy Glen, "Operation of the aerodynamic plasma actuator at high altitude" (2012). *Masters Theses*. 6867.
https://scholarsmine.mst.edu/masters_theses/6867

OPERATION OF THE AERODYNAMIC PLASMA ACTUATOR AT HIGH ALTITUDE

by

TIMOTHY GLEN NICHOLS

A THESIS

Presented to the Faculty of the Graduate School of the

MISSOURI UNIVERSITY OF SCIENCE AND TECHNOLOGY

In Partial Fulfillment of the Requirements for the Degree

MASTER OF SCIENCE IN AEROSPACE ENGINEERING

2012

Approved by

Joshua L. Rovey, Advisor
Serhat Hosder
Fathi Finaish

ABSTRACT

A plasma actuator was operated at altitudes from 0 to 18288 meters to determine the mechanisms leading to decreased force production at low pressures. The actuator was driven with a 5 kHz sine wave and a peak to peak voltage of 13.4 kV at pressures of 760, 429, 321, 226, and 88 Torr. A passive measurement technique called the capacitive V-dot probe was adapted to the actuator in order to resolve the spatiotemporal evolution of the surface potential and electric field on the dielectric surface. At low pressures up to 20 times more plasma is present than at atmospheric conditions. Average force production is calculated and shown to decrease at lower pressures due to the fact that up to 88% of the plasma is created in regions where the electric field is approximately zero. The calculated average body force shows a slight increase up to a pressure of 429 Torr before trending to zero at lower pressures. Performing a power analysis shows that as pressure is decreased more power is used creating plasma than accelerating it, leading to a decrease in efficiency.

ACKNOWLEDGMENTS

I would first like to thank my advisor, Dr. Joshua Rovey, for all of his help and guidance throughout my years at S&T. Without his understanding and encouragement I would not have completed this thesis. I would also like to think Dr. Serhat Hosder and Dr. Fathi Finaish for serving as my committee members as their advice and help with this project have been greatly appreciated.

I would also like to thank all of the students in the Aerospace Plasma Lab: Jing, Steve, Ryan, Alex, Mark, Andrew, and Warner. The help I received with my project from everyone was fantastic and helped me more than some of you may know. Also, the conversations we have had (academic and non-academic alike) have been a great pleasure of mine since joining the lab.

Finally, I'd like to thank my family (Tina, Sam, and Jonathan Nichols) and my girlfriend, Meagan Kreps. Though you probably understood little to nothing of my research when I spoke of it, serving as a frustration vent was more help than even I realized until now. Even more, you believed in me to accomplish my goals and to live out a dream and for that I will be forever thankful.

TABLE OF CONTENTS

SECTION

APPENDICES

LIST OF ILLUSTRATIONS

NOMENCLATURE

Symbol	Description
C_1	capacitance between exposed electrode and dielectric surface $[F]$
C_2	capacitance between the dielectric and the buried electrode $[F]$
C_3	capacitance due to geometric arrangement of plasma actuator $[F]$
C_{int}	op-amp integrator capacitor value $[F]$
d	dielectric material thickness $[mm]$
e	electric charge $[C]$
ε_r	dielectric constant
ε_o	permittivity of free space $[\frac{C^2}{Nm^2}]$
E	electric field $[\frac{V}{mm}]$
$\vec{F}$	induced force $[N]$
I	current $[A]$
K_1	calibration factor due to charging of bulk capacitance $\left[\frac{V}{kV}\right]$
K_2	calibration factor due to charging of dielectric surface $\left[\frac{V}{kV}\right]$
K_3	calibration factor due to polarization charging of dielectric surface
n_i	ion density $\left[\frac{number\ of\ ions}{mm^3}\right]$
N	number of samples
P	power $[W]$
V	plasma volume $[\frac{1}{m^3}]$
R_{int}	op-amp integrator resistor value $[\Omega]$

σ	surface charge density $\left[\frac{C}{m^2}\right]$
V_{ac}	applied voltage $[kV]$
V_{probe}	V-dot probe signal $[V]$
V_{surf}	surface potential due to charge deposition $[kV]$
V_{net}	total surface potential on dielectric surface $[kV]$
V_{Max}	potential due to capacitive voltage division and polarization $[kV]$

1. INTRODUCTION

This introductory section provides an overview of single dielectric barrier discharge (SDBD) plasma actuators, operating characteristics of the actuator, and recent research performed.

1.1. DBD ACTUATOR INTRODUCTION

Single dielectric barrier discharge plasma actuators have shown promise as reliable and easy to use active flow control devices [1-4] **.** The induced flow that the actuator produces has been shown to delay stall and separation over an airfoil, in turn maintaining lift at high angles of attack [2, 5-8]. SDBD plasma actuator parameters such as material thickness, type of dielectric material used, applied waveform shape and frequency, and actuator geometry have been shown to affect the discharge characteristics and therefore the effectiveness of the actuator [9-13].

The SDBD plasma actuator consists of a dielectric material and two electrodes arranged in an asymmetrical geometry as shown in Figure 1.1. Copper tape is most commonly used for the electrodes, while glass, Kapton tape, Teflon, and Macor ceramic are commonly used as the dielectric material. One electrode is placed on the dielectric surface exposed to ambient air conditions, while the other electrode is grounded and covered by a dielectric material on the opposite side of the dielectric. These electrodes are referred to as the exposed and buried electrodes, respectively. To operate an actuator, a high frequency high voltage AC waveform (from a few kilovolts to tens of kilovolts; frequencies in the kHz range) is applied between the electrodes.

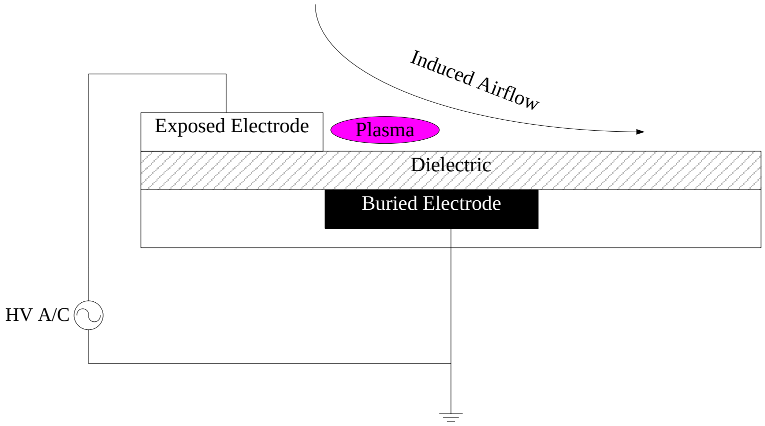

Figure 1.1: Schematic diagram of a DBD plasma actuator. The actuator controls the air flow by inducing a body force on the fluid.

1.2. DBD ACTUATOR OPERATION

During normal operation of the plasma actuator, the plasma ignites and extinguishes twice during the applied waveform period. The first half cycle, called the forward stroke, is when the voltage applied on the exposed electrode is negative going. During this half of the cycle electrons are transferred from the electrode to the dielectric surface. These electrons collide with neutral air particles creating ions and forming the plasma. The plasma then quenches and the voltage goes from being negative to positive. During the back stroke, or positive-going voltage, electrons are drawn back to the exposed electrode from the dielectric surface. They again collide with neutral air particles causing the second ignition of the plasma. The plasma quenches again when the voltage is no longer positive-going. As plasma ions are created they are simultaneously accelerated downstream by the electric field present between the electrodes. Ions transfer momentum to the surrounding neutral air molecules through collisions creating an induced flow tangential to the dielectric surface. This flow is the mechanism for aerodynamic control by the actuator. Momentum transfer collisions occur close to the dielectric surface, usually in the sub-boundary layer region. Gregory et al. have shown that the body force produced by a plasma actuator is due to the acceleration of plasma ions through an applied electric field and the subsequent collisions with neutral particles [14]. This force is governed by ion density and the applied electric field, as shown in Eq. (1).

$$< \vec{F} > = \int \int e n_i(\vec{r}, t) \vec{E}(\vec{r}, t) d\vec{r} dt \tag{1}$$

1.3. PREVIOUS RESEARCH ON DBD ACTUATORS AT HIGH ALTITUDE

The amount of force produced by a SDBD plasma actuator depends heavily on a number of parameters mentioned previously. The environment in which the actuator operates is one of the most influential factors affecting overall performance. Operating a plasma actuator in a low pressure environment leads to an increase in power consumption, a larger plasma formation region, and an induced flow velocity that increases initially, but then decreases [14-21]. Gregory et al. found a linear relationship between force production and the ambient atmospheric conditions, with the force going to zero in vacuum conditions [14]. They also found a nonlinear relationship between electric field strength and pressure, attributing the decrease in field strength as pressure decreases to the variation of breakdown voltage as the neutral density changes. Similar results regarding the change in the average electric field were found by Litvinov et al.[15]. They also demonstrated that there is an increase in force production down to pressures of 200 Torr due to an increase in the volume of the plasma. This leads to an increase in the number of plasma ions available for momentum transfer. Following this study, Benard et al. used pitot tube measurements to show that the induced velocity increases as the pressure drops from 760 Torr, where the velocity is 2.5 m/s, down to 456 Torr, where the velocity is 3.5 m/s [16, 17]. Pressures below 456 Torr show the induced velocity decreasing. Another study performed by Benard et al. found an increase in electric wind velocity down to pressures of 350 Torr at which point the induced velocity began decreasing [16]. An increased mass flow rate can be achieved down to pressures of 350 Torr by increasing the grounded electrode length, but at lower pressures this affect becomes greatly reduced. A study performed by Wu et al. produced results that show a maximum induced velocity of approximately 1.5 m/s at 445 Torr, which is in good agreement with Benard et al. [17, 18]. They also showed that below 45 Torr the plasma formed on the dielectric surface switches from a filamentary dominated discharge to a glow dominated discharge. Abe et al. demonstrated the highly non-linear fashion in which ambient pressure affects the induced velocity and thrust generated [19]. Their work shows an increase in thrust as the pressure drops to approximately 600 Torr before trending to zero. Another study performed by Benard and Moreau also showed that a decrease in pressure results in increased power consumption as well as an increase in induced flow velocity from 3 m/s at 760 Torr to 5 m/s at 287 Torr.

To gain a better understanding of the fundamental operation of the plasma actuator it is necessary to study the correlation between operating parameters and the plasma actuator characteristics. In this study the actuator is operated in a simulated high altitude environment in order to understand the effects of low pressure on the overall charge deposition, dielectric surface potential, electric field strength, and fundamental force production mechanisms.

2. EXPERIMENTAL TECHNIQUES AND SETUP

This section provides an overview of how the experiment is set up and carried out as well as the details for each piece of equipment used. Specifically, this section covers the operation of a V-dot probe and its calibration, plasma actuator construction, V-dot probe electronics, and the high altitude testing chamber.

2.1. BASIC PLASMA ACTUATOR OPERATION

Understanding the experimental procedure requires an understanding of how charge buildup on the dielectric surface leads to plasma formation. The discharge mode of the DBD exists as discrete microdischarges, not as one continuous discharge [4]. These microdischarges deposit charge onto the dielectric surface which reduces the applied electric field at that particular location. This limits the region of expansion of the plasma and is the cause for its self-limiting behavior. Furthermore, the structure of the plasma has been shown to be vastly different between the forward and backward strokes [22]. The electric potential at the exposed electrode is well-defined since it is equal to the applied potential. Likewise, the potential on the buried electrode is known (in this configuration it is the ground reference). The potential build-up on the surface of the dielectric, however, depends on two things: the capacitance division that is inherent in the actuator design and the surface-plasma interaction [23, 24]. Even when there is no breakdown and plasma does not form, the presence of some non-zero potential is present due to the polarization effect of the dielectric. In order to determine the potential on the dielectric surface as a function of space and time we use a series of capacitive V-dot probes (shown in Figure 2.1).

To determine the potential on the dielectric surface as a function of time and space, the buried electrode is broken into 14 electrically isolated segments (shown in Figure 2.1) which are grounded through an op-amp based active integrator circuit, as opposed to being grounded directly (shown in Figure 2.2) . An electrically isolated segment combined with an active integrator circuit make-up what is called a V-dot probe. Each V-dot probe is 2.5 mm x 5 cm with the entire array of 14 probes arranged in a staggered formation. Since the plasma extent grows as the ambient pressure decreases, the probe array is spaced such that the surface potential and electric field far from the exposed electrode edge can be calculated.

The numbered probes in Figure 2.1 correspond respectively to downstream distances of $x =$ 1.00, 2.25, 3.50, 4.75, 7.50, 9.75, 12.50, 14.75, 20.00, 24.75, 30.00, 34.75, 40.00, and 44.75 mm. To keep cross-talk between the individual probes at a minimum one V-dot probe is used at a time. This signal is passed through the vacuum chamber via a BNC-BNC pass through while the other 13 probes are shorted directly to ground. In this way the surface potential is stitched together from running the actuator at the same operating condition 14 different times. To ensure that the plasma discharge propagates downstream as it would with an un-segmented buried electrode, the copper surrounding the V-dot probes is also grounded.

The integrator circuit sums the current that is due to the charging of the bulk capacitance as well as the current that charges the dielectric surface. The former of these effects does not contribute to the surface potential buildup on the dielectric which is why it is necessary to calibrate the circuit response for each of these effects separately. This is done through two different calibrations, described in the following sections.

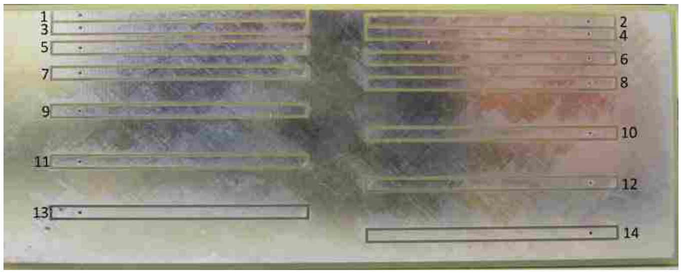

Figure 2.1: The spacing of the V-dot probes is such that at low pressures the charge on the dielectric surface can be measured over the entire extent of the plasma, not just close to the exposed electrode.

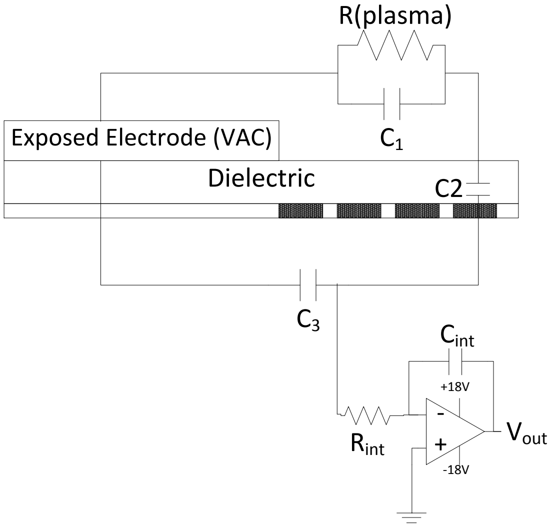

Figure 2.2: Each buried segmented electrode is connected to an op-amp based integrator circuit with a large resistor in parallel (50 MΩ in this experiment) with the integrating capacitor, C_{int}.

2.2. ANALYSIS OF A CAPACITIVE V-DOT PROBE

An analysis of any one of the signals from a particular op-amp integrator circuit is performed in the following steps. Using the first calibration factor, K_1, the displacement current due to bulk charging is subtracted from the raw signal received from circuit. The remaining current is due to the physical charge deposition onto the dielectric surface.

Using the second calibration factor, K_2, it is possible to determine the surface potential due to this charge buildup. Letting $V_{probe,i}(t)$ be the signal from the ith probe, the surface potential at a probe location, $V_{surf,i}(t)$, due to charge accumulation on the dielectric surface with an applied waveform $V_{ac}(t)$ is given by Eq. 2. The total surface potential, $V_{net,i}(t)$, is then found by adding $V_{surf,i}(t)$ to the surface potential due to the capacitive voltage division/polarization effect of the dielectric material, V_{Max}, as is shown in Eq. 3. The amount of charge that is physically deposited onto the surface of the dielectric is readily calculated using Eq. 4.

It is important to note that the op-amp integrator signal is an integral over time with respect to an initial starting condition. Therefore, it is necessary to start each measurement from a known starting condition, that is, an uncharged dielectric surface. To achieve this, a solvent (in this experiment, acetone) is used to wipe the surface of the actuator to remove the long living DC charge [26] that exists between runs of the actuator.

$$V_{surf,i}(t) = \frac{V_{probe,i}(t) - K_1 V_{ac}(t)}{K_2} \tag{2}$$

$$V_{net,i}(t) = V_{surf,i}(t) + V_{Max} \tag{3}$$

$$\sigma_i = (\frac{\varepsilon_r \varepsilon_o}{d}) V_{surf,i} \tag{4}$$

2.2.1. Charging of the Bulk Capacitance – 1st Calibration. Production of the SDBD body force that allows for flow control comes from the creation and acceleration of ions. The acceleration of the ions occurs due to an electric field that originates at the exposed electrode and terminates on the buried electrode. Due to the geometry of the plasma actuator, it is necessary to include the capacitance C_3 (shown in both Figure 2.2 and Figure 2.3). This is because some electric field lines pass through the dielectric material and terminate on the buried electrode, directly connecting the two electrodes and providing a parallel path for additional displacement current to flow. It should be noted that although this current is always present in the circuit, it does not affect the overall plasma discharge. This capacitance does not contribute to the surface charging of the dielectric surface. Since the integrator circuit produces a signal that is due to the displacement current through all three of the capacitances shown in Figure 2.3, the portion of the signal from the integrator circuit that is due to the charging of C_3 must be subtracted off. This value (referred to as the “bulk capacitance”) requires running the actuator at a low voltage (less than the required voltage needed to generate plasma.) Doing this for each V-dot probe comprises the 1st calibration and gives the calibration factor, K_1, for each probe. The response of a given probe to an applied waveform is linear to within ± 0.3%, shown in Figure 2.4. For a pressure of 760 Torr we find that K_1 varies from $K_1 = 0.348$ V/kV for the probe nearest the exposed electrode to $K_1 = 0.007$ V/kV at the probe farthest from the exposed electrode, as shown in Figure 2.5. Since the actuator geometry and operating parameters remain constant, it is expected that the same value for K_1, regardless of the ambient pressure, will be observed. This is indeed what we find with the largest deviation being ± 0.18% for the probe nearest the exposed electrode.

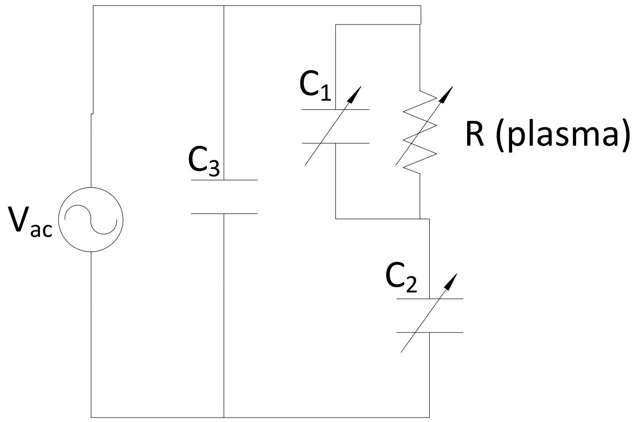

Figure 2.3: Lumped circuit model of the DBD plasma actuator (from Enloe et al. [1]).

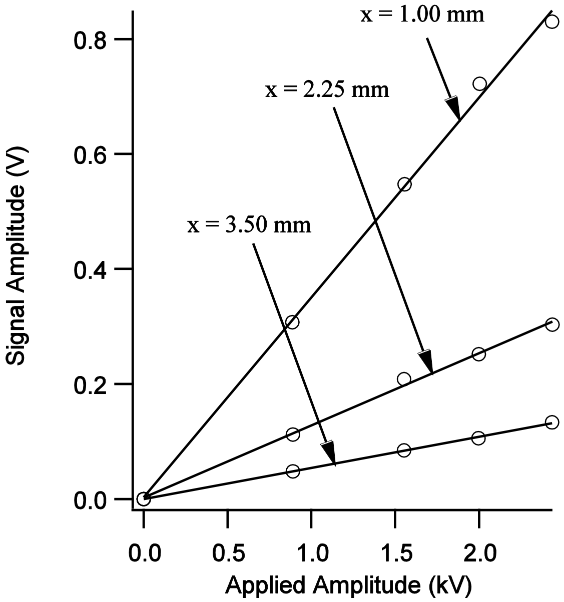

Figure 2.4: The response of the V-dot probe to the charging of the "bulk capacitance" is linear.

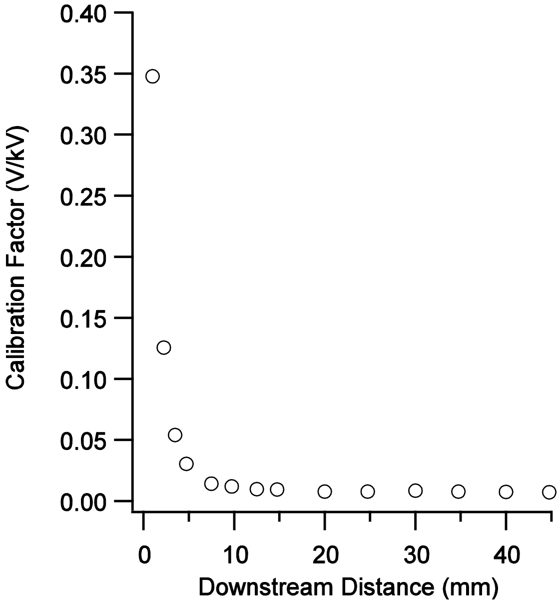

Figure 2.5: The 1st calibration factor ranges from K_1 = 0.348 V/kV at the closest probe to 0.007 V/kV at the farthest probe.

2.2.2. Surface Charging – 2nd Calibration. Whereas the first calibration takes into account the displacement current that goes into charging the bulk capacitance, the second calibration is used to determine the amount of charge physically deposited on the dielectric surface by the plasma. In Figure 2.3, C_1 is the capacitance between the exposed electrode and the dielectric surface. The capacitance C_2 is located between the dielectric surface, which serves as a virtual electrode, and the buried physical electrode. Since the plasma extent in the downstream direction changes during operation, the capacitances C_1 and C_2 will as well; this is why they are represented as variable elements in Figure 2.3. At breakdown (i.e. when plasma is present), a resistive path (R) becomes present from the exposed electrode to the dielectric surface. This current cannot penetrate the dielectric material (unlike the current in the first calibration). In keeping with the current literature [24] this volume is broken into two different capacitances, labeled C_1 and C_2 in Figure

2.3. With plasma present current flows through R charging C_1 which creates another displacement current that the integrator circuit will measure. It is possible to determine the V-dot probe response to this displacement current by running the actuator at low voltages with a temporary extension of the exposed electrode over the dielectric surface. The extended electrode serves to mimic the effect of surface potential due to charge buildup on the surface. This extension of the exposed electrode is realized by covering the surface of the dielectric with copper tape. This calibration factor relates the V-dot probe output voltage to the charge accumulation on the dielectric surface. Since each probe in this experiment has identical dimensions the second calibration factor should be the same for each V-dot probe. This is what we find with K_2 at atmospheric conditions being $K_2 = 0.257$ V/kV where the percent difference between all probes is ± 9.7%.

2.2.3. Charge Due to Capacitive Voltage Division and Polarization of Dielectric Material. Using the first and second calibrations and Equation 2 it is possible to determine the amount of charge being deposited on the dielectric surface. The total potential on the dielectric surface, however, is due not only to the deposited surface charge, but also to the polarization created by the dielectric surface. Additionally, the applied potential on the exposed electrode is capacitively divided by C_1 and C_2 even when plasma is not present. Accounting for this is straight forward and is calculated by solving Laplace’s equation with the appropriate boundary conditions. The program Ansoft Maxwell is used to perform these calculations and provides the unit-less third calibration factor, K_3. The value of K3 ranges from $K_3 = 1$ right at the exposed electrode edge to $K_3 = 0.00205$ at the last V-dot probe. By adding the contributions to the potential from the polarization effect and deposited charge on the dielectric surface, the total potential on the dielectric surface at 14 different spatial locations can be determined (Eq. 3). Using these data it is then possible to determine the electric field downstream from the exposed electrode.

2.3. PLASMA ACTUATOR

The plasma actuator used in this study has a standard asymmetrical geometry between the exposed and encapsulated electrode with a 1.6 x 305 x 305 mm piece of Macor ($\varepsilon_r = 6$) between them. The dimensions of the exposed electrode are 0.2 x 138 x 17.3 mm. The buried electrode has a total downstream length of 52 mm with 14 electrically isolated V-dot probes that have dimensions of 2.5 mm x 5 cm. By using the spacing shown in Figure 2.1 it is possible to measure the potential on the dielectric surface up to 44.75 mm downstream from the exposed electrode. Additionally, by using a Tektronix P6015 high voltage probe to measure the potential on the exposed electrode a fifteenth data point in the potential distribution across the dielectric surface can be determined. A picture of the actuator used in this experiment is shown in Figure 2.6.

A simple block diagram showing the components of the actuator electrical system is shown in Figure 2.7. Operation of the plasma actuator uses a Rigol DG 1022 function generator which is connected to a Crown CE 2000 amplifier. The signal from the amplifier is stepped up to kilovolt level with a CMI-5525 high frequency transformer. This transformer has a turn ratio of 1/357, a frequency range of 900 Hz – 5 kHz, and is capable of outputting up to 25 kV at 0.2 Arms.

A Pearson 4100 current monitor, placed around the common ground wire, is used to measure the total actuator current. It has a 10 ns rise time which, for this application, is accurate enough to measure the displacement current as well as to capture the microdischarge current spikes produced by the actuator that are indicative of plasma formation.

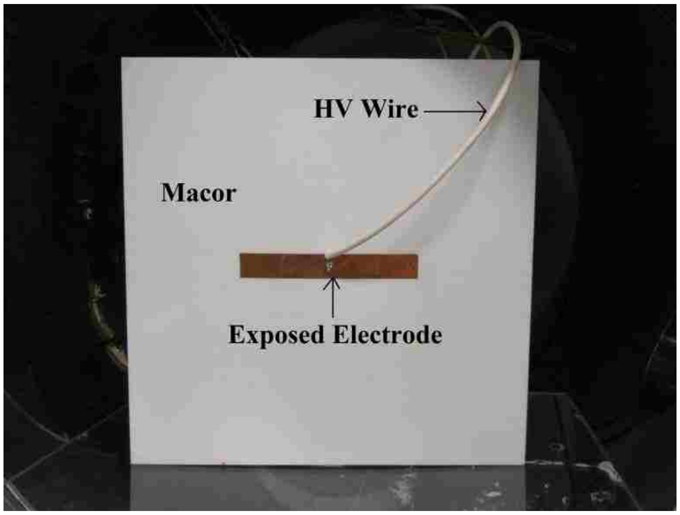

Figure 2.6: The large Macor dielectric provides enough surface area to prevent arcing at low pressures.

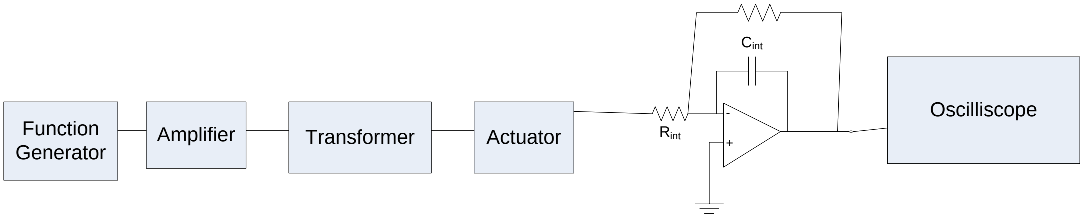

Figure 2.7: A 5 kHz sine wave is generated with the function generator and then stepped up through an amplifier and step-up transformer to kV levels. The integrator circuit output is fed to an oscilloscope.

2.4. V-DOT PROBE ELECTRONICS

The op-amp integrator circuit has a LF-411 op amp with C_{int} = 11 nF. A large resistor (in this experiment 50 MΩ) is placed in parallel with C_{int} such that the capacitor is completely bled off in between runs. This is important because the integrator must start from some known (i.e. uncharged) state. The RC time constant for this circuit is 550 ms, which is much slower than the 0.2 ms applied waveform period. With this time constant and a known starting condition all aspects of the integrator circuit are valid, including the DC offset that occurs during the first period of the applied AC waveform.

Each V-dot probe is connected to ground (or the integrator circuit if being tested) with standard RG-58 coaxial cable and terminated with a 50 Ω BNC connector. The grounded shield of the cable is used to eliminate cross talk between the V-dot probes as well as decrease noise. The probes that are shorted directly to ground are connected to a conducting box and grounded to the vacuum chamber (discussed below), which serves as the common ground for the entire experiment. Standard coaxial cable is again used to establish the ground connection between the grounding box and the common ground due to its low impedance characteristics.

2.5. HIGH ALTITUDE TESTING SETUP

The entire experimental setup is shown in Figure 2.8. The high voltage wire from the step-up transformer connects to a high voltage pass through into the bell jar vacuum chamber. The ambient pressure is measured with a Lesker KJL275800 convection pressure gauge which has a range of 1000 - 10^{-4} Torr. The signal from a single V-dot probe is connected to a BNC pass through and connected to an integrator circuit. A

Tektronix DPO 2024 oscilloscope is used to measure and record all waveform data. A Tektronix P6015 high voltage probe, with a 1000:1 step down for the given experiment impedance, is used to measure the voltage being applied to the exposed electrode. This also serves as a 15th data point in our knowledge of the spatiotemporal potential deposition on the dielectric surface. A faraday cage houses the step-up transformer as well as the high voltage probe.

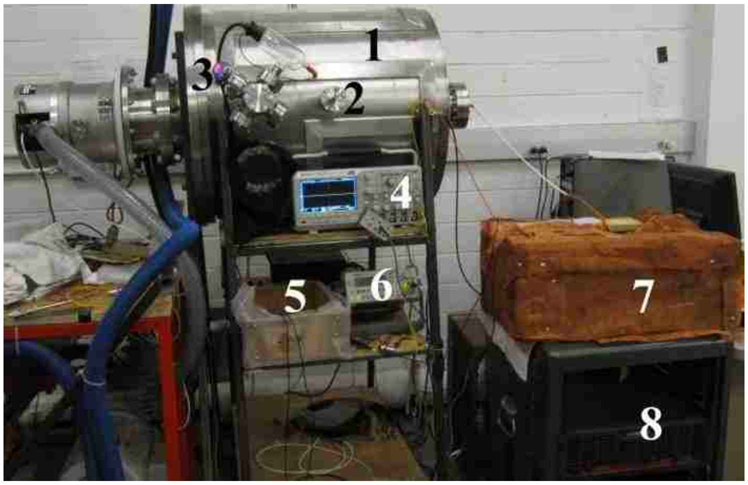

Figure 2.8: 1. Vacuum Chamber; 2. BNC-BNC Passthrough; 3. Lesker Pressure Gauge; 4. Tektronix DPO 2024 Oscilliscope; 5. Op-Amp Integrator Circuit; 6. Rigol Function Generator; 7. Faraday Cage; 8. Crown Amplifier.

3. RESULTS

Results from studies on the effect of pressure on plasma extension, power consumption, surface potential, longitudinal electric field, and plasma density are presented here. Surface potential and longitudinal electric field calculations from V-dot probe data are shown. The time-averaged light intensity measurements of the plasma are also presented. A power analysis is also performed on the actuator at each operating pressure.

3.1. PLASMA EXTENSION AND POWER CONSUMPTION

Power dissipation by the actuator at different pressures was determined by operating the actuator with the same input parameters (13.4 $kV_{pk\text{-}pk}$, 5kHz frequency) and varying the pressure. Using Eq. (5) and the current and voltage waveforms shown in Figure 3.1 we calculate the time averaged (over four periods of the applied waveform) power dissipation. The results are shown in Figure 3.2, where the power per unit length is based on the width of the buried electrode. With three different sets of data we determine that the average power varies, at most, by 20% for a given operating pressure. This is indicated by the error bars in Figure 3.2. At 760 Torr the power consumed by the actuator is approximately 0.2 W/cm whereas at the lowest tested pressure of 88 Torr, the actuator draws 1.1W /cm. The non-linear increase in power as pressure decreases matches the trends seen by Benard *et al.* [16, 17].

$$P = \frac{1}{N}\sum_{i=1}^{N} I_i V_i \tag{5}$$

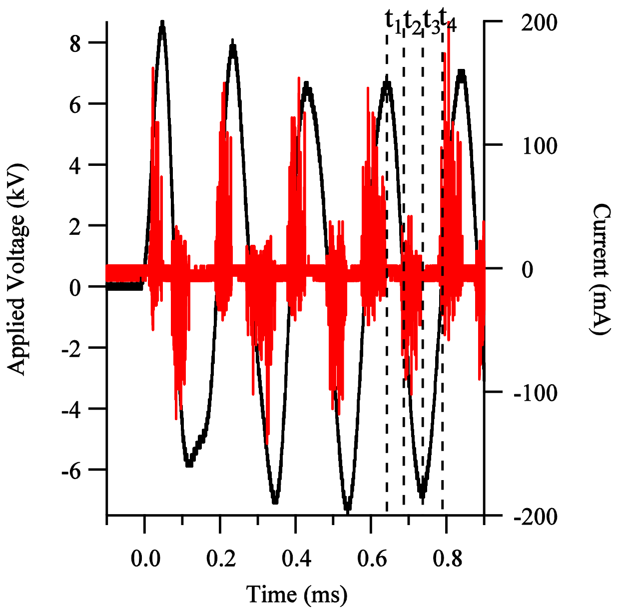

Figure 3.1: Applied waveform (black) and corresponding current plot (red) with four distinct time intervals labeled.

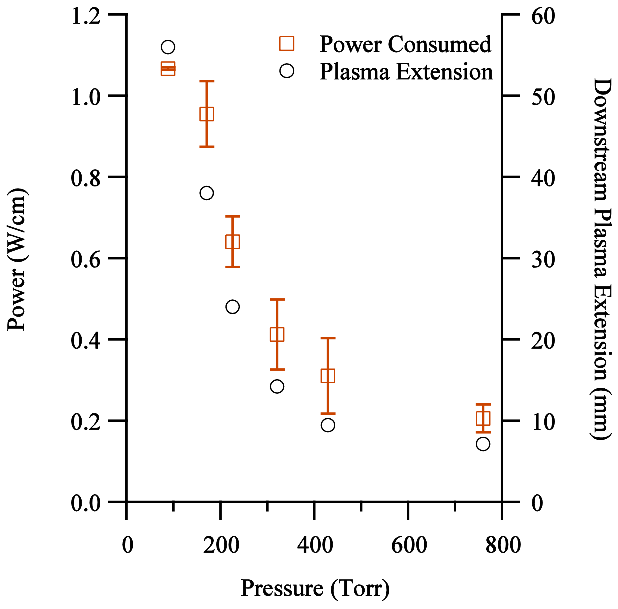

Figure 3.2: Decreasing the pressure increases power consumption and also causes plasma to form farther downstream.

In order to determine the effect that pressure has on the extent of the plasma formation region, qualitative photographs, such as those shown in Figure 3.3, are used. The exposure time for each picture was set at 1/3 s providing a time averaged photograph of the distribution of plasma on the surface of the dielectric. These results are shown in Figure 3.2 and indicate a non-linear growth in the plasma extension as pressure decreases. These results agree well with those presented by Benard et al.[16, 17]. It is also worth noting that as the pressure decreases more plasma is also formed on the upstream side of the exposed electrode. In other words, plasma is formed where there is no grounded electrode. Even at 760 Torr, plasma is formed on the corners of the exposed electrode in the upstream direction due to the strong electric fields that are present at the points of the electrode edge. Finally, the extent of the plasma has surpassed the length of the buried electrode (52 mm) at 88 Torr.

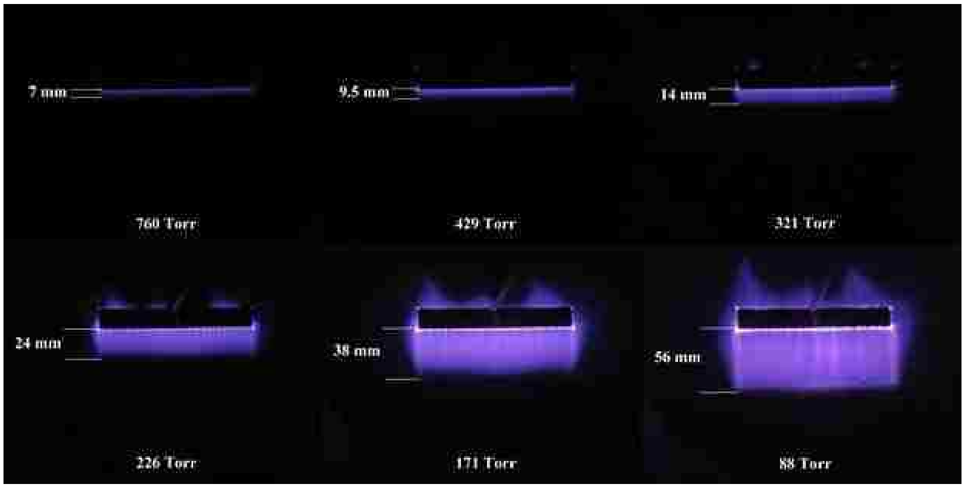

Figure 3.3: Pictures taken with 1/3s exposure time show the time averaged plasma distribution on the dielectric surface.

3.2. SURFACE POTENTIAL AND ELECTRIC FIELD MEASUREMENTS

Results in this section were obtained by applying Eq. (2) and (3) with the previously discussed calibrations to the raw V-dot probe measurements. All data were obtained for the first few cycles of the applied waveform with a clean actuator (surface wiped with acetone between shots). To reiterate, wiping the surface of the dielectric ensures that the displacement current being integrated by the integrator circuit is due solely to the plasma discharge and not to residual charge left from previous plasma shots.

In Figure 3.4-Figure 3.9, the surface potential is plotted as a function of time and downstream distance. These plots provide an overview of the surface potential distribution and behavior. At 760 Torr the surface potential is highest closest to the exposed electrode. As pressure decreases the surface potential begins to spread out across the dielectric surface. This is indicative of more plasma being formed in the downstream location. Further evidence of this is the fact that in the peak surface potential decreases near the exposed electrode while downstream locations that had a surface potential of approximately zero (at 760 Torr) increase as pressure is lowered. This suggests that the electrons emitted from the exposed electrode (in the forward stroke; from the dielectric surface on the backward stroke) can travel greater distances before having collisions with neutral air or being deposited on the dielectric surface (as the mean free path increases with decreasing pressure).

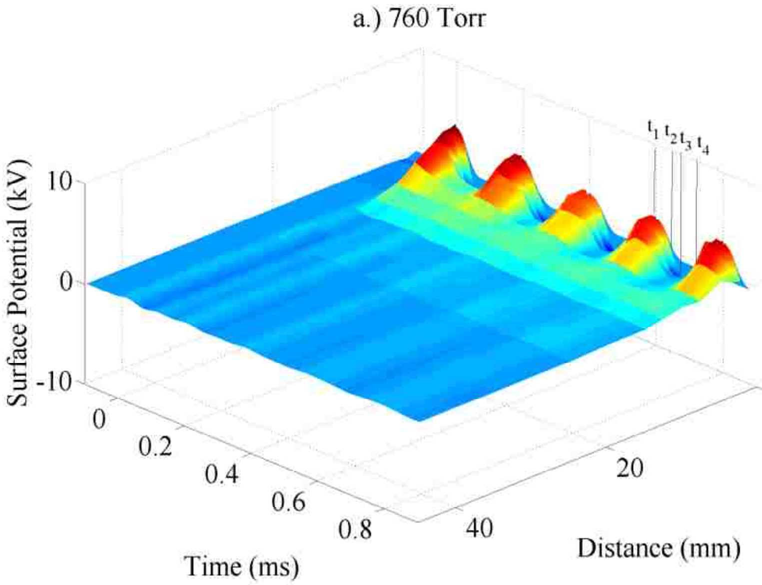

Figure 3.4: 3D plot of surface potential as a function of downstream position and time at 760 Torr.

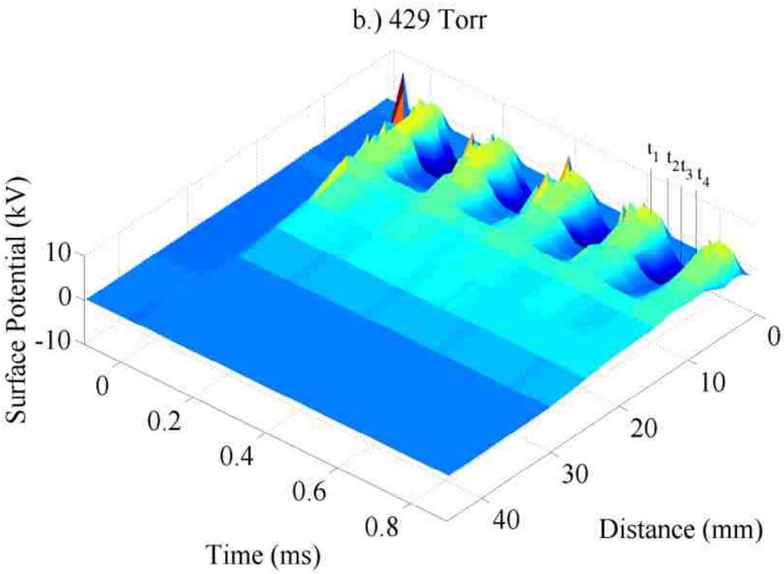

Figure 3.5: 3D plot of surface potential as a function of downstream position and time at 429 Torr.

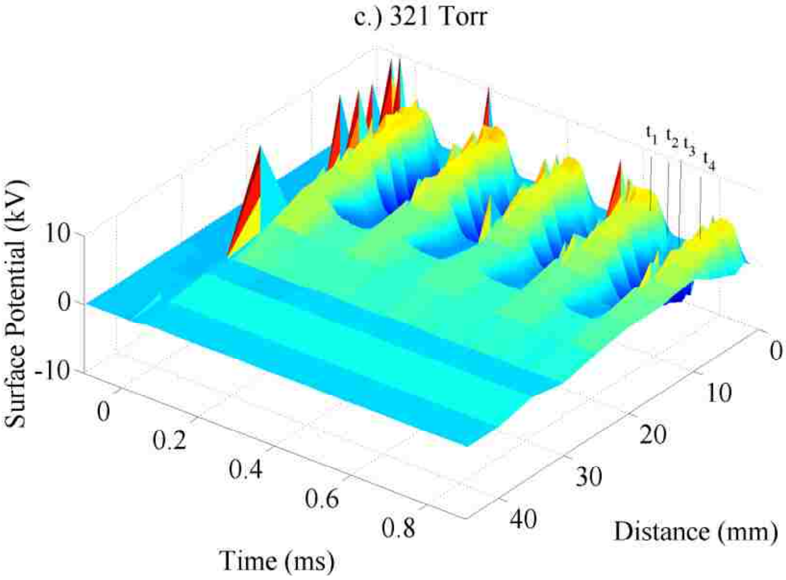

Figure 3.6: 3D plot of surface potential as a function of downstream position and time at 321 Torr.

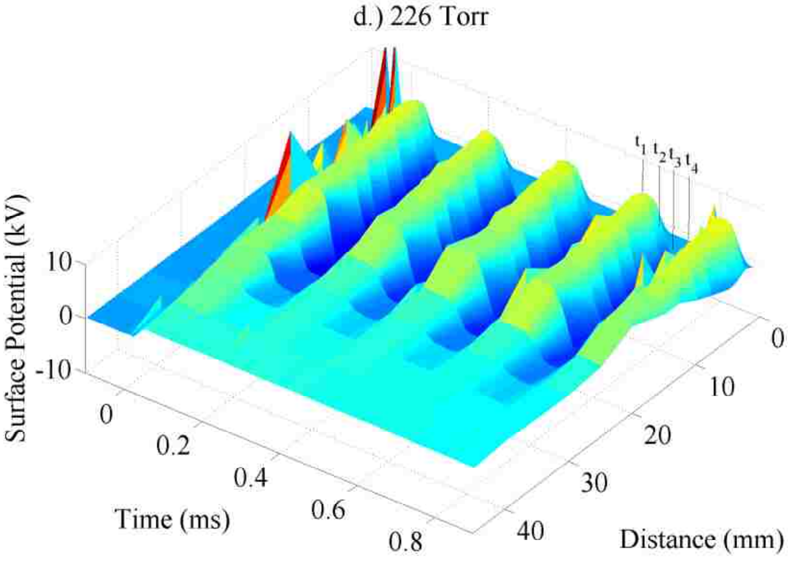

Figure 3.7: 3D plot of surface potential as a function of downstream position and time at 226 Torr.

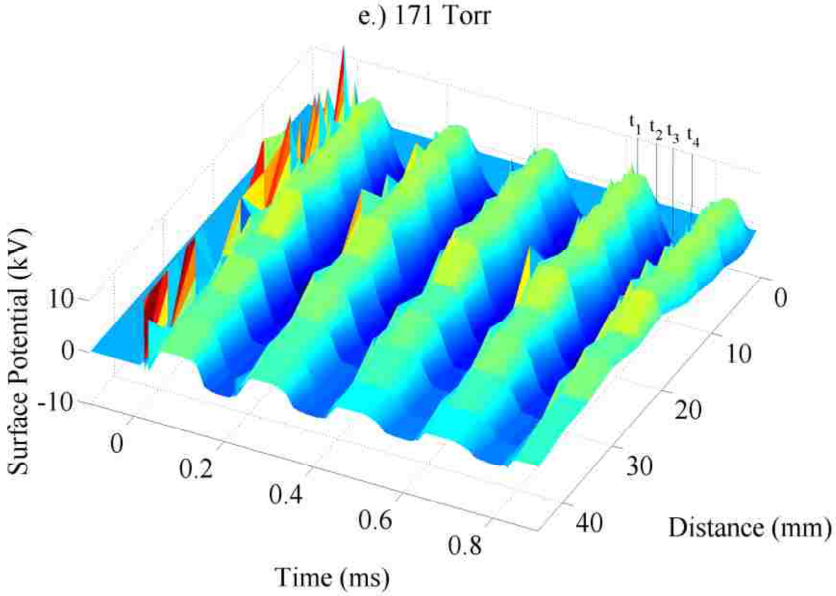

Figure 3.8: 3D plot of surface potential as a function of downstream position and time at 171 Torr.

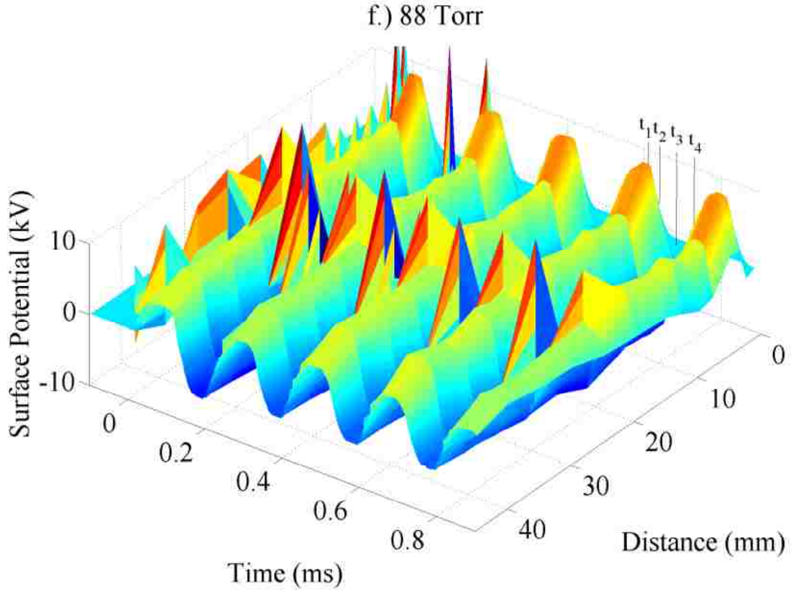

Figure 3.9: 3D plot of surface potential as a function of downstream position and time at 88 Torr.

While looking at the three-dimensional plots provides a good overview of the surface potential, it is more beneficial to examine the surface potential distribution in discrete slices of time. These plots can be seen in Figure 3.10- Figure 3.57, where the surface potential and corresponding longitudinal electric field are plotted for each operating pressure. The time intervals shown in these figures correspond to the times labeled in Figure 3.1. Time t_1 corresponds to when the plasma is quenched and the change in applied potential is negative. As the applied waveform progresses the plasma ignites in the forward stroke at approximately time t_2 (50 μs after t_1). The plasma quenches again at time t_3 (100 μs after t_1), before it enters the backward stroke and ignites for the second time at t_4 (150 μs after t_1). By looking at the surface potential at the four described time intervals it is possible to see how charge is deposited on the dielectric surface as the actuator progresses through each of the four distinct phases of operation.

The results of operating the actuator at atmospheric conditions are shown in Figure 3.10 **-** Figure 3.17. In Figure 3.10 the plasma is quenched at the peak amplitude of the applied waveform (t_1). During this time, the surface potential at all downstream locations is positive. The potential between 2 and 5 mm is unchanged until the potential trends to zero far away from the exposed electrode edge. The change in surface potential close to the exposed electrode is due to the capacitive voltage division and polarization charge on the dielectric surface. The longitudinal electric field derived from the data shown in Figure 3.10 is shown in Figure 3.11. Worth noting is the large span of dielectric surface (from 5 to 14 mm) where the electric field is roughly constant at $E \approx 0.2$ kV/mm. As the plasma ignites at time t_2 (Figure 3.12), the effects of negative charges being carried downstream by the plasma can be seen. As in Figure 3.10**,** there is a large region of net positive surface potential from approximately 3 mm and on with a corresponding region of positive electric field (Figure 3.13) at 7 mm. During this part of the discharge cycle, the strongest electric field is limited close to the exposed electrode edge (≈ 2 mm and closer). At t_3 (Figure 3.14 and Figure 3.15) the plasma is again quenched and we can see similarities between the t1 interval and the t_3 interval. A region of positive surface potential is again established at 5 mm and remains positive as the surface potential trends to zero far from the exposed electrode. The electric field varies the most at 7 mm and closer, but remains unperturbed farther downstream where there is no discharge. The plasma reignites in the final phase of the discharge cycle (t_4) and is shown in Figure 3.16 and Figure 3.17. The maximum electric field shown in Figure 3.17 is larger than that shown in Figure 3.13 (1.25 kV/mm and 1.8 kV/mm, respectively) due to the fact that although the applied waveform is symmetric, the surface charge density is not.

In Figure 3.18-Figure 3.25, the results for 429 Torr are presented. During time t_1 the surface potential shown in Figure 3.18 follows similar trends to those found in Figure 3.10.The surface potential follows that of the applied voltage for distances approximately 2 mm and closer to the exposed electrode. The surface potential trends to zero outside the region of constant surface potential between 2 and 5 mm. The longitudinal electric field (Figure 3.19) does not appear to be constant between 2 mm and 14 mm as is the case in Figure 3.11. This same region, however, exhibits a local maximum of $E \approx 0.5$ kV/mm before trending to zero. When the plasma ignites at t_2 the effects of decreased pressure can immediately be seen (Figure 3.20 and Figure 3.21). When compared with Figure 3.12, the magnitude of the surface potential at each distinct time step is similar, however the distance downstream that experiences an always net positive surface potential now begins at 5 mm, whereas before the region of positive surface potential began at 3mm. This is evidence that as the plasma sweeps out farther downstream from the exposed electrode at lower pressures the deposited charge is also swept farther downstream. The electric field (Figure 3.21) shows a similar shift with a positive electric field being generated from 9 mm before trending to zero. The magnitude of the electric field is approximately the same when compared with the results from 760 Torr. As the plasma is quenched at t_3 (Figure 3.22and Figure 3.23) the similarities to time t_1 can again be seen. A region of positive surface potential is established from 5 mm before trending to zero far from the exposed electrode. The electric field becomes positive at 10 mm, much like during the t_2 interval, before trending to zero. When compared with Figure 3.15the magnitude of the electric field remains approximately the same. During the t_4 interval, shown in Figure 3.24and Figure 3.25, the plasma ignites for the second time and again the effect of the decrease in pressure can be seen. The region of positive surface potential is established 5 mm, just as in t_2. The electric field remains constant from 11 mm and farther, before trending to zero far away from the exposed electrode. The magnitude of the electric field is smaller during t_4 than in t_2 for the same reasons discussed previously.

The results shown in Figure 3.26- Figure 3.33 are obtained by operating the actuator at a pressure of 321 Torr. Unlike the 760 Torr case, during the t_1 time interval the surface potential does not follow the applied potential close to the exposed electrode, but instead remains constant or shows a slight increase up to 4 mm (Figure 3.26). The electric field (Figure 3.27) remains constant at $E \approx 0.2$ kV/mm between 5 and 44.75 mm. When the plasma ignites at t_2, the plasma now (visually) sweeps out to approximately 14 mm (as shown in Figure 3.3). This can be seen in the surface potential shown in Figure

3.28. Like the 760 Torr case, there is a region in which the dielectric surface acquires an always net positive surface potential starting at 7.5 mm and continuing over the entire dielectric surface. The electric field during this time interval (Figure 3.29) becomes positive at 20 mm and is relatively constant at E ≈ 0.1 kV/mm. When the plasma again quenches, similar trends emerge that were seen during t_1. The surface potential (Figure 3.30) becomes positive at 13 mm and reaches a maximum value of 3.5 kV before trending to zero. The electric field (Figure 3.31) during this time interval remains constant over all time slices after 20 mm. At positions closer to the exposed electrode ($x < 5$ mm) the electric field increases at first (up to 2.5 mm) before entering a region of negative electric field between 5 and 22.5 mm. When the plasma ignites for the second time (Figure 3.32 and Figure 3.33) there is a positive, non-zero surface potential between 12.5 and 40 mm, similar to that of t_2. The electric field during this time interval oscillates from zero and 0.05 kV/mm between 20 and 44.75 mm. Note that the overall electric field strength is weaker at this pressure when compared to the 760 Torr case discussed previously.

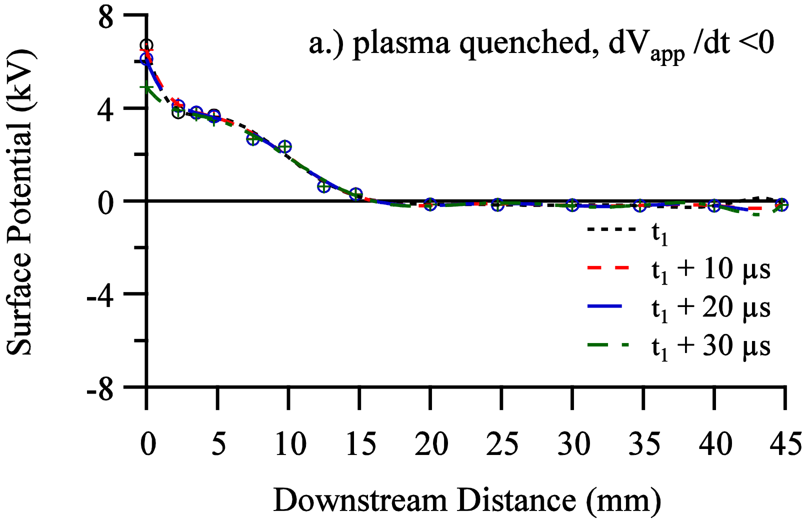

Figure 3.10: Potential on the surface of the dielectric between t_1 and t_2 at 760 Torr.

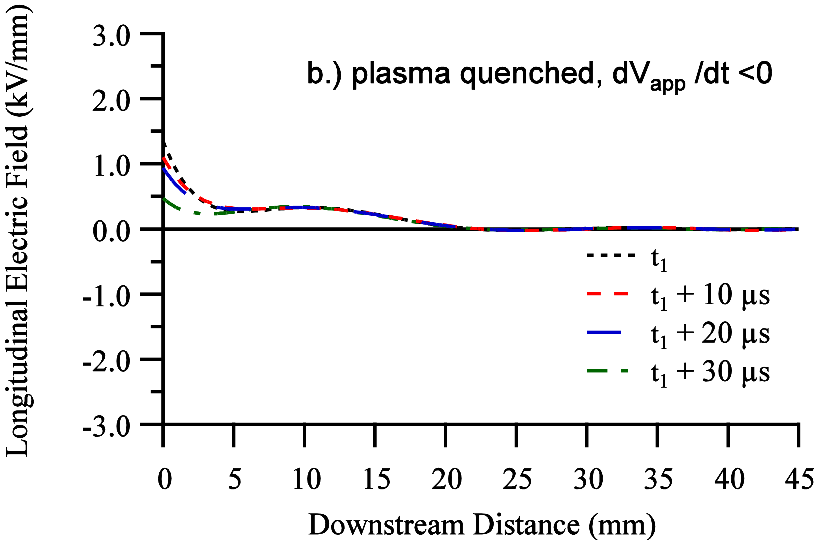

Figure 3.11: Electric field near the dielectric surface between t_1 and t_2 at 760 Torr.

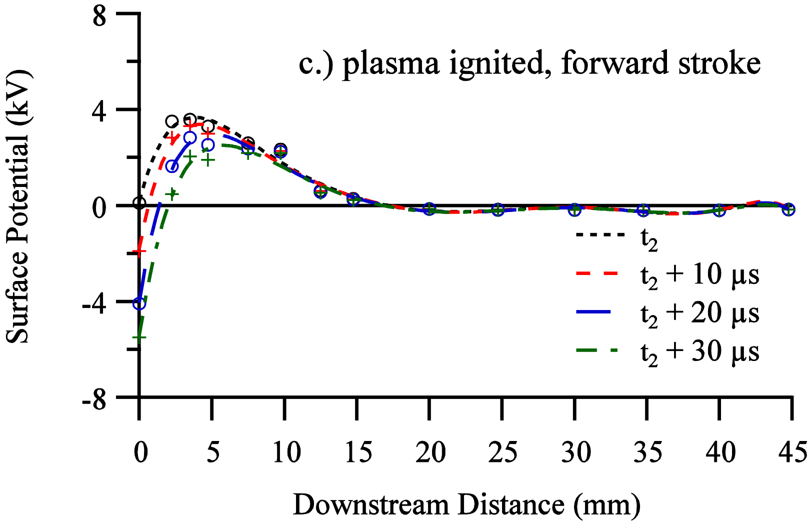

Figure 3.12: Potential on the surface of the dielectric between t_2 and t_3 at 760 Torr.

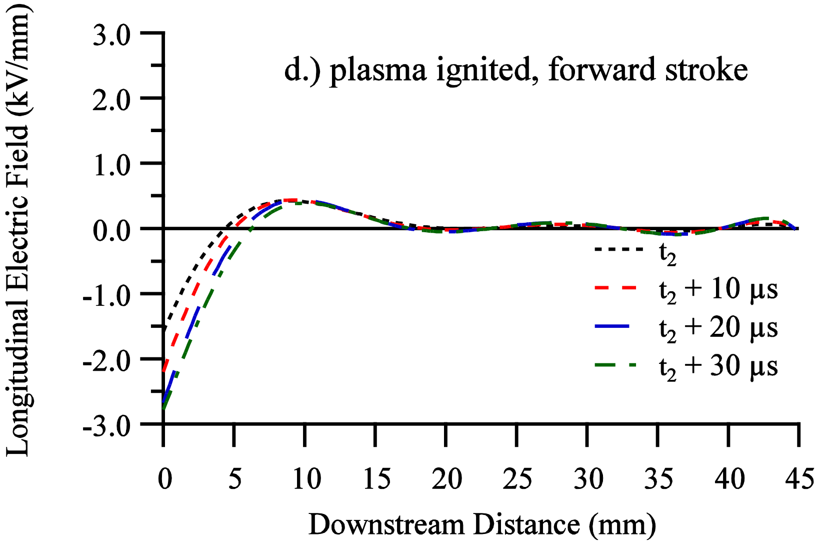

Figure 3.13: Electric field near the dielectric surface between t_2 and t_3 at 760 Torr.

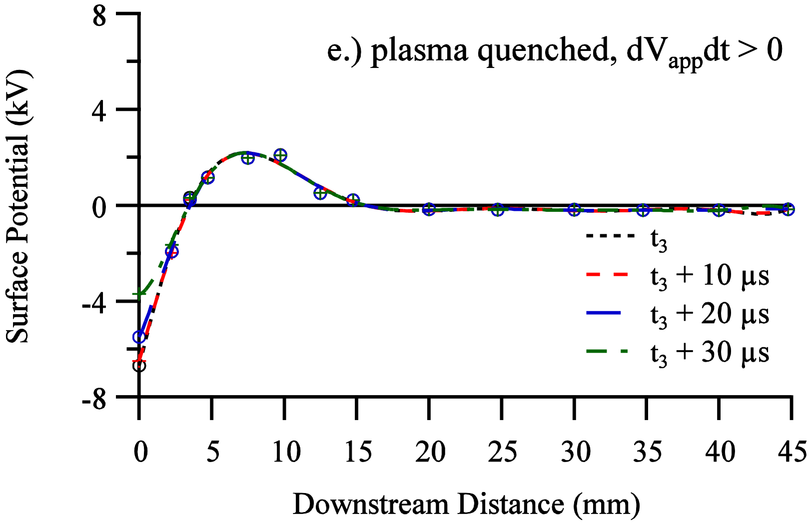

Figure 3.14: Potential on the surface of the dielectric between t_3 and t_4 at 760 Torr.

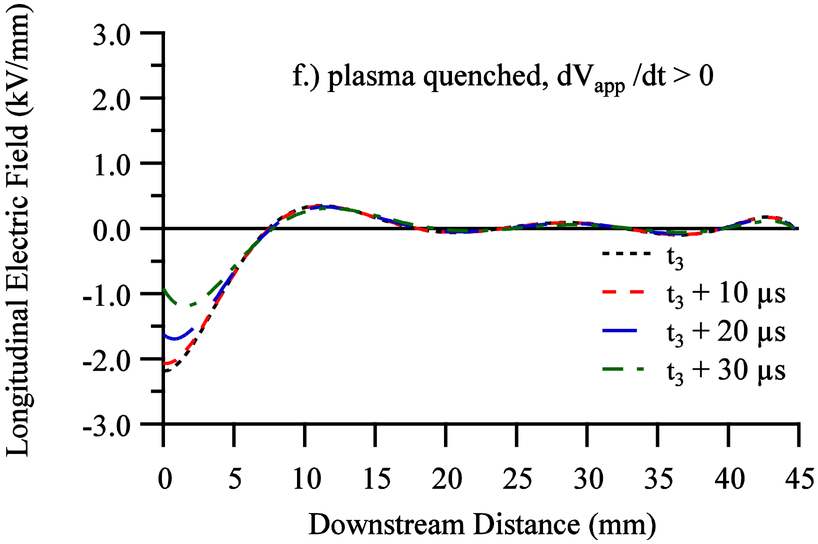

Figure 3.15: Electric field near the dielectric surface between t_3 and t_4 at 760 Torr.

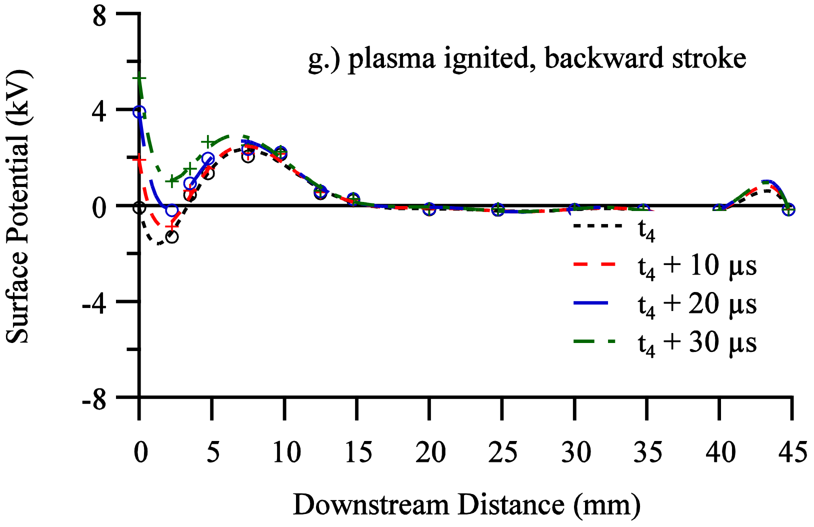

Figure 3.16: Potential on the surface of the dielectric after t_4 at 760 Torr.

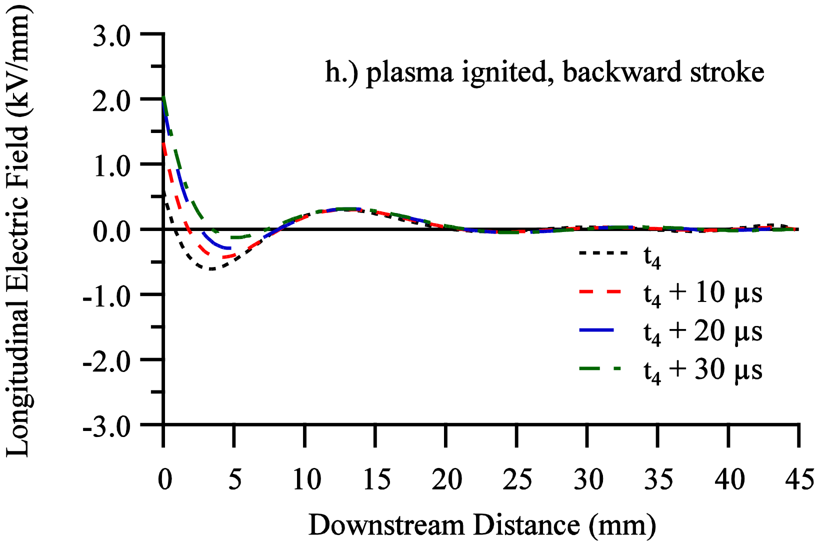

Figure 3.17: Electric field near the dielectric surface after t_4 at 760 Torr.

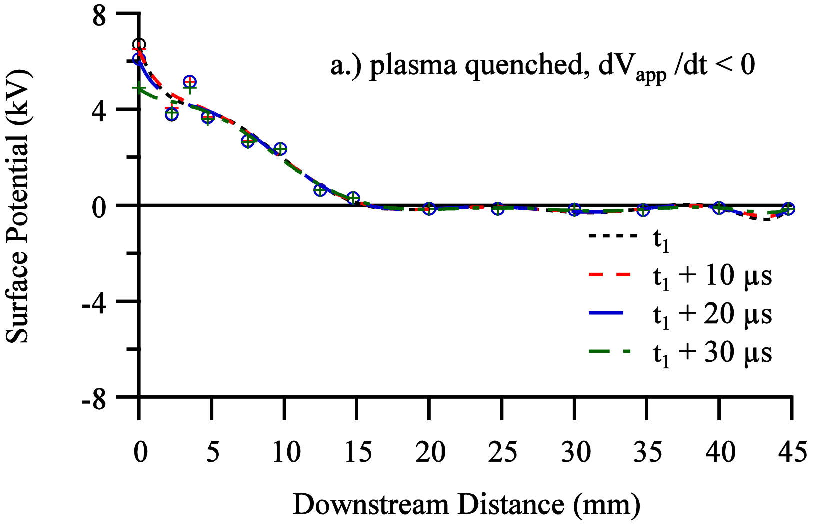

Figure 3.18: Potential on the surface of the dielectric between t_1 and t_2 at 429 Torr.

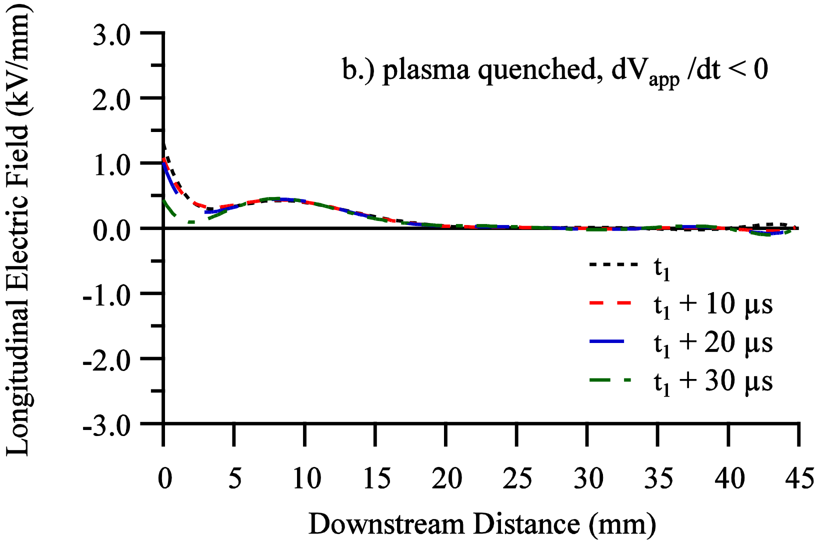

Figure 3.19: Electric field near the dielectric surface between t_1 and t_2 at 429 Torr.

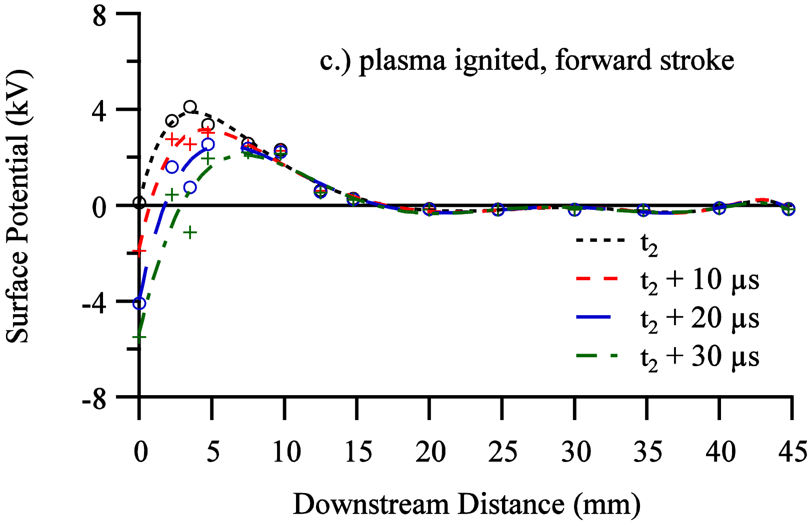

Figure 3.20: Potential on the surface of the dielectric between t_2 and t_3 at 429 Torr.

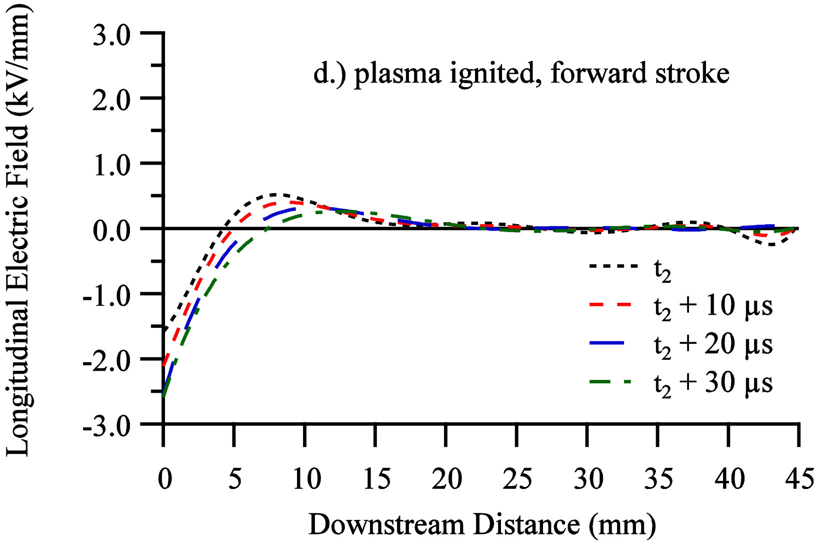

Figure 3.21: Electric field near the dielectric surface between t_2 and t_3 at 429 Torr.

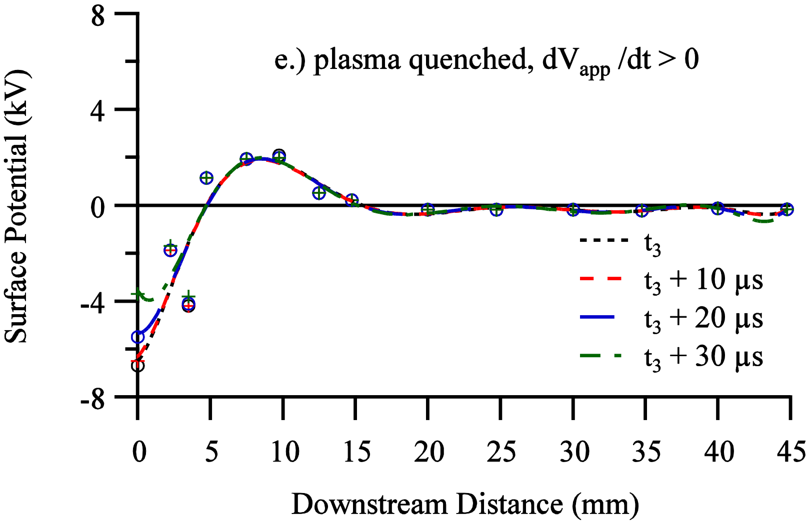

Figure 3.22: Potential on the surface of the dielectric between t_3 and t_4 at 429 Torr.

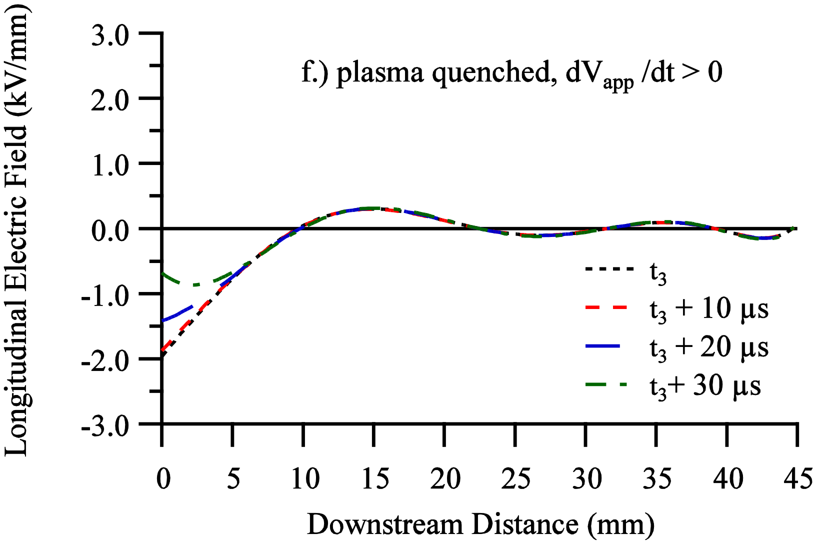

Figure 3.23: Electric field near the dielectric surface between t_3 and t_4 at 429 Torr.

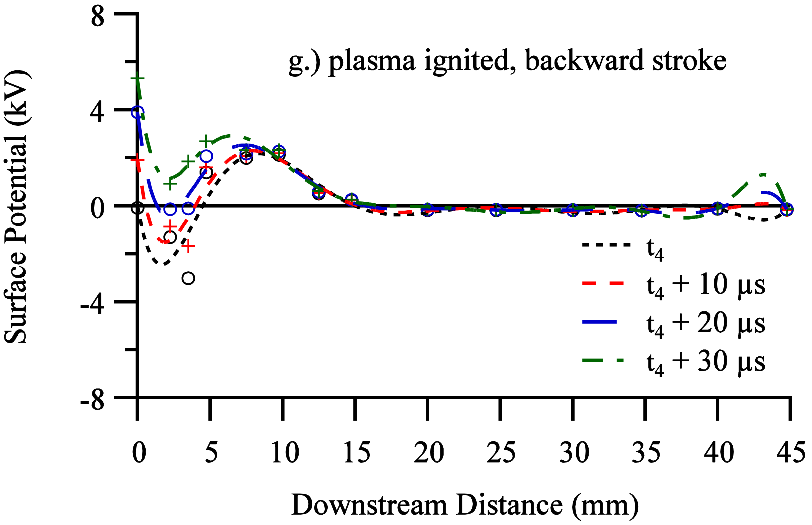

Figure 3.24: Potential on the surface of the dielectric after t_4 at 429 Torr.

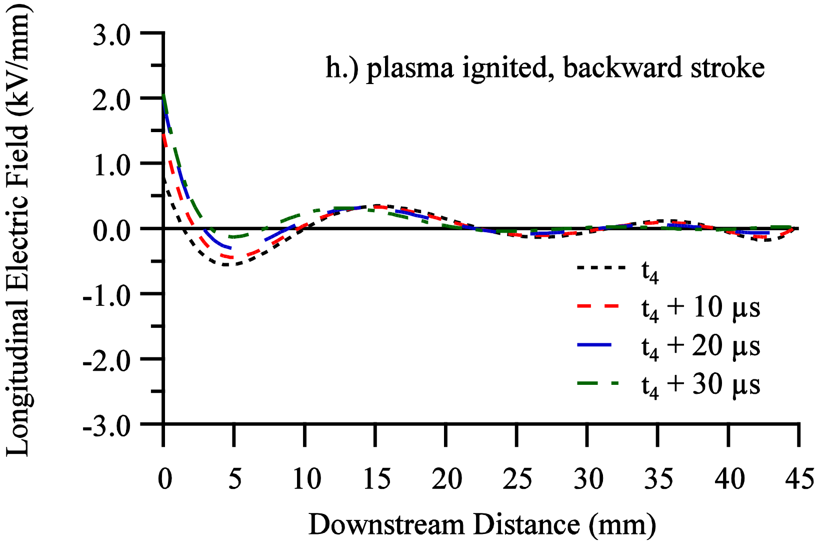

Figure 3.25: Electric field near the dielectric surface after t_4 at 429Torr.

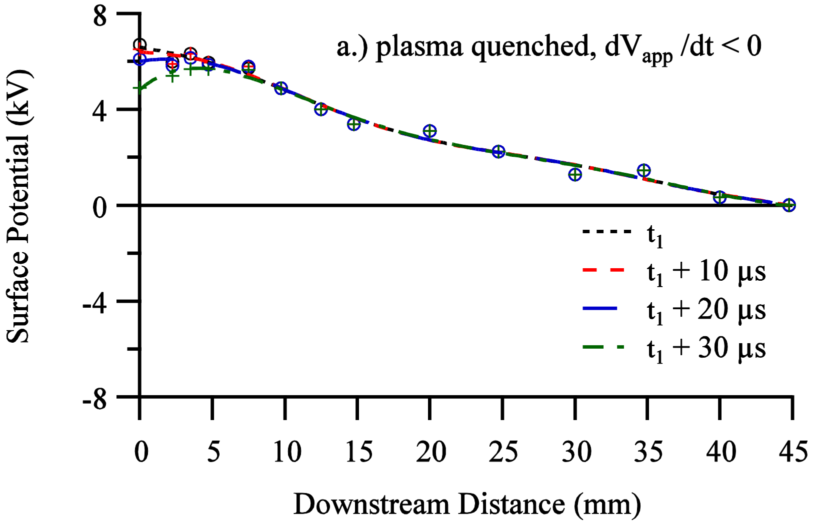

Figure 3.26: Potential on the surface of the dielectric between t_1 and t_2 at 321 Torr.

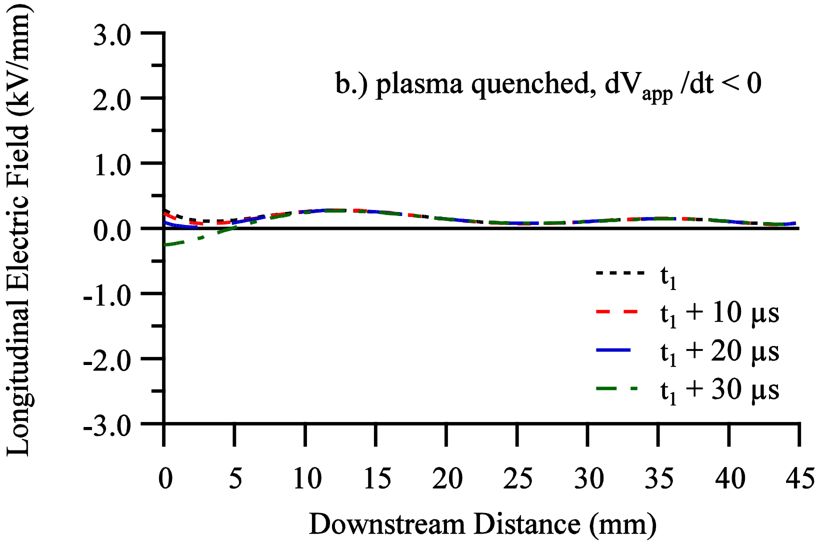

Figure 3.27: Electric field near the dielectric surface between t_1 and t_2 at 321 Torr.

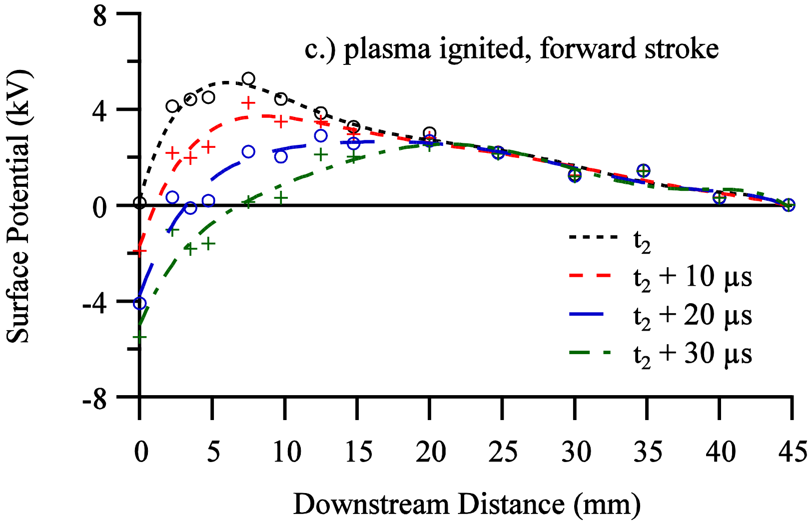

Figure 3.28: Potential on the surface of the dielectric between t_2 and t_3 at 321 Torr.

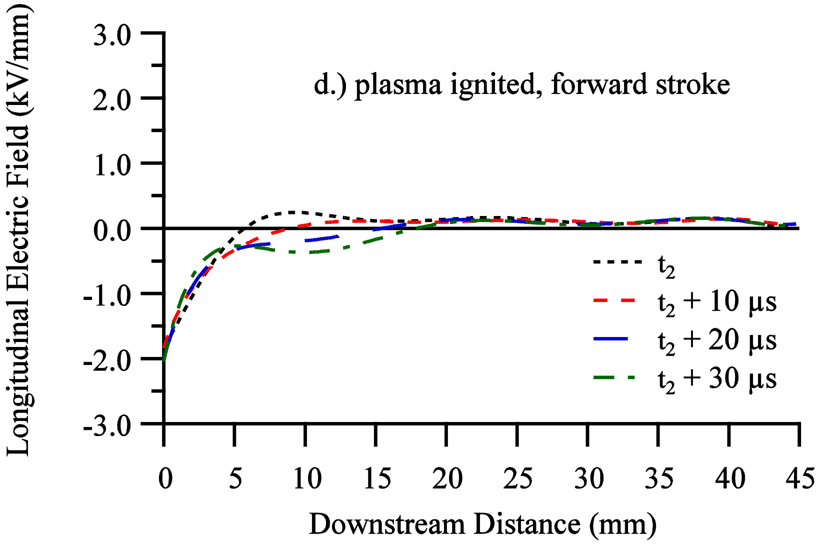

Figure 3.29: Electric field near the dielectric surface between t_2 and t_3 at 321 Torr.

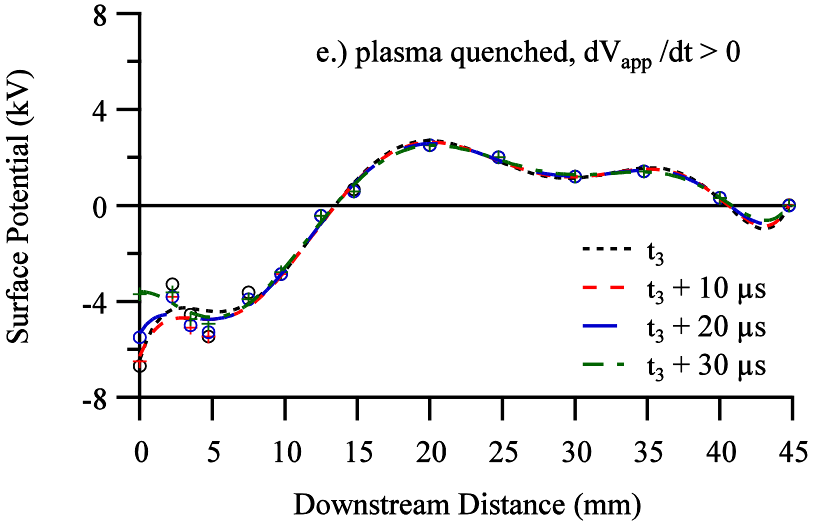

Figure 3.30: Potential on the surface of the dielectric between t_3 and t_4 at 321 Torr.

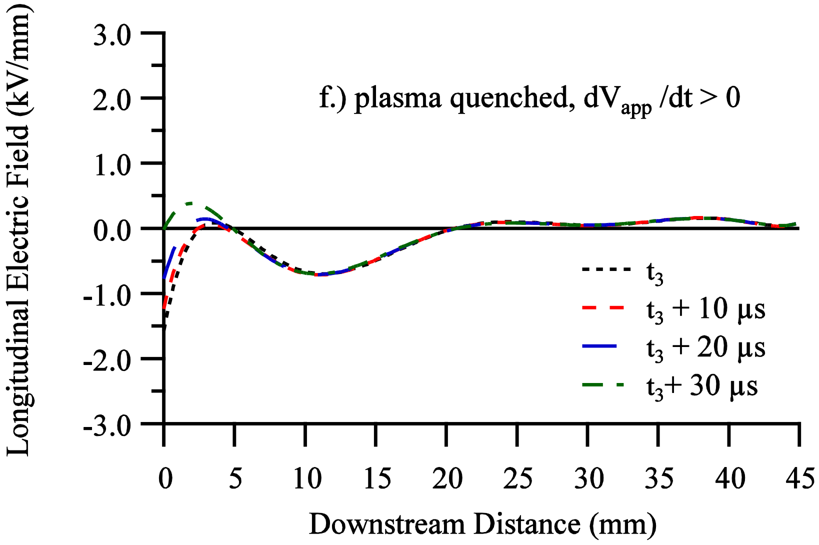

Figure 3.31: Electric field near the dielectric surface between t_3 and t_4 at 321 Torr.

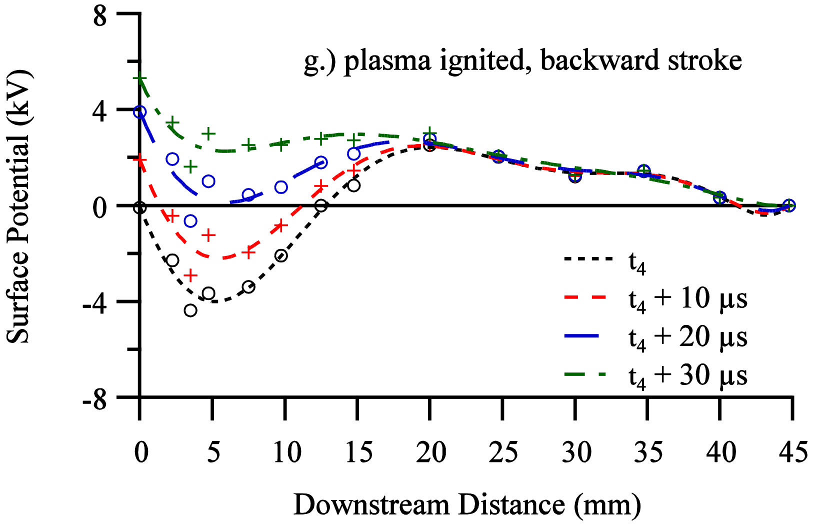

Figure 3.32: Potential on the surface of the dielectric after t_4 at 321 Torr.

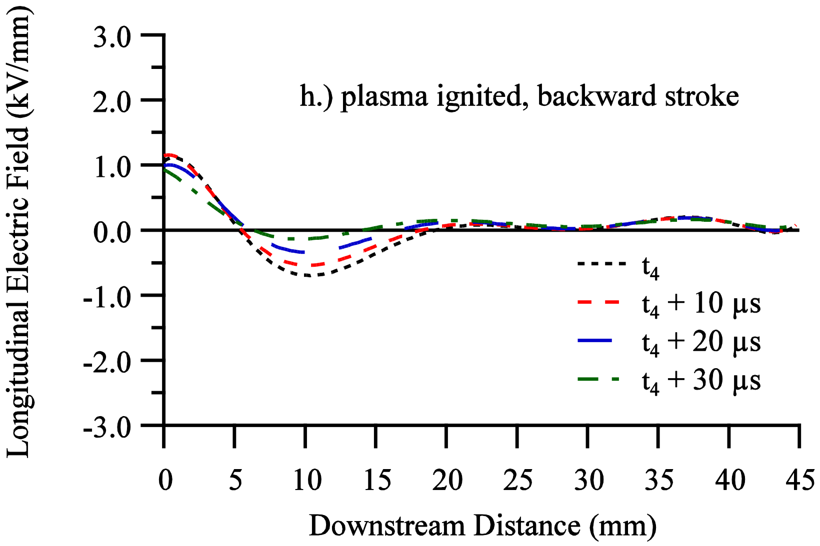

Figure 3.33: Electric field near the dielectric surface after t_4 at 321 Torr.

Plotted in Figure 3.34- Figure 3.41 are the results of operating the actuator at a pressure of 226 Torr. During t_1 the surface potential exhibits all of the previously discussed trends and, like the results at 321 Torr, increases up to a distance of 10 mm. At this pressure, however, the surface potential never goes to zero and always has a value of 2 kV or greater. The electric field (Figure 3.35) is uniform over the entire dielectric surface (except at 7 mm or less) at a magnitude of E ≈ 0.1 kV/mm before going to zero at 40 mm. When the plasma ignites at t_2 (Figure 3.36) the spread of surface potential between time slices is larger than the previously discussed pressures. The potential increases up to a value of 6 kV and after 15 mm is always positive and non-zero. The corresponding electric field is approximately constant after 10 mm, varying slightly between zero and 0.10 kV/mm. During time t_3 similar trends discussed for t_1 are seen in the surface potential. The region of positive potential is established after 27.5 mm whereas at 321 Torr the region of positive surface potential was established at a distance of 15 mm. The electric field at this time shows similar trends to those discussed for Figure 3.35. Here, however, the electric field is constant from 7 mm to 30 mm with E ≈ -0.3 kV/mm. The electric field never returns to a positive value before going to zero at 44.75 mm. This is the first time that the electric field is largely negative over the entirety of the dielectric surface. When the plasma ignites for the second time, a region of constant positive surface potential is established at 27.5 mm. The surface potential never goes to zero far away from the exposed electrode edge, maintaining a value of 2 kV at 44.75 mm while the electric field is largely negative between 10 mm and 35 mm.

When the plasma is quenched during t_1 at a pressure of 171 Torr (Figure 3.42 and Figure 3.43) the surface potential remains constant at 6 kV out to a distance of 20 mm before beginning to decrease. The electric field is approximately zero from 5 mm until the end of the buried electrode. A local maximum of E = 0.2 kV/mm at a downstream distance of 25 mm is seen, but this is an artifact of the fitting routine used on the data.

Once the plasma ignites the effect the plasma has on sweeping the charge across the dielectric surface is readily seen (Figure 3.44). A region of always positive surface potential is established at 30 mm. The electric field (Figure 3.45) remains mostly constant throughout this time interval, oscillating between 0.5 kV/mm and -0.5 kV/mm. At t_3 there is never a region on the dielectric surface where the surface potential (Figure 3.46) is always positive. The electric field exhibits a local maximum at 2.5 mm downstream, but then trends to zero. The electric field between 6 and 17 mm is approximately zero before going negative between 17 and 44.75 mm (see Figure 3.47). Between all of the time intervals the surface potential, as well as the electric field, does not vary much. In Figure 3.48 and Figure 3.49 the effect the plasma has on the distribution of the surface potential is seen again. During each time step between 10 and 30 mm, the surface potential remains constant. The electric field decreases from 1.5 kV/mm to zero by 5 mm and remains approximately zero over the entirety of the dielectric surface.

At a pressure of 88 Torr, the same trends when the actuator is operating at a pressure of 171 Torr are seen during each of the time intervals. During t_1 (Figure 3.50 and Figure 3.51) there is a region between 5 and 25 mm that has a constant surface potential of 6 kV. The electric field during this time interval is zero after 5 mm. Similar trends to that shown at 171 Torr are seen again as the plasma ignites at t_2 (Figure 3.52 and Figure 3.53).When the plasma quenches again at t_3 (Figure 3.54 and Figure 3.55) the surface potential is constant at -6 kV over nearly all of the dielectric surface, only beginning to increase at a downstream location of 35 mm. Just like in the case of 171 Torr, there is no region of positive surface potential that is established on the dielectric surface. Again, the electric field has a non-zero value only close to the exposed electrode edge before going to zero at 10 mm. Once the plasma forms for the second time (Figure 3.56 and Figure 3.57) the plasma sweeps the charge across the dielectric, remaining constant for each time interval between 5 and 45 mm. At t_4 + 10 μs the surface potential remains positive across the dielectric surface, with an approximately constant value of 1.75 kV. The electric field exhibits similar behavior as that shown in the time interval of t_2. Polarization effects are seen close to the exposed electrode edge, but the majority of the dielectric surface experiences an electric field of zero. The electric field does take on a small negative magnitude at 35 mm, however the overall trend cannot be captured due to the lack of V-dot probes after 44.75 mm.

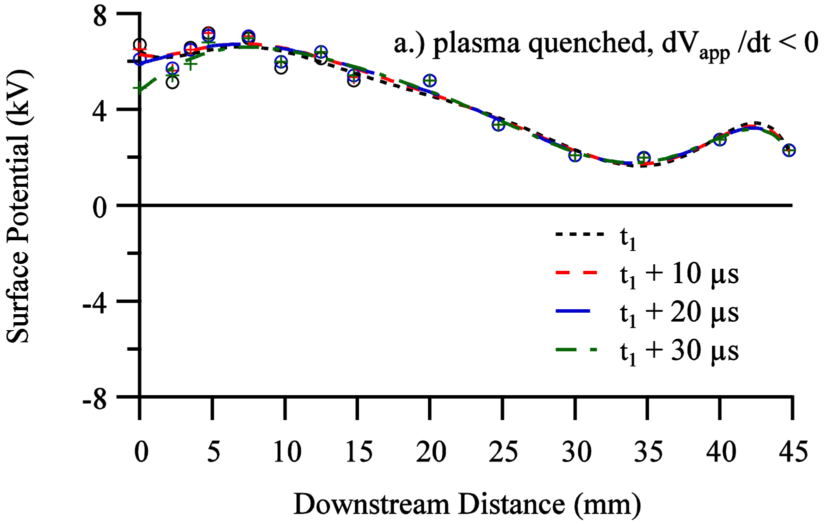

Figure 3.34: Potential on the surface of the dielectric between t_1 and t_2 at 226 Torr.

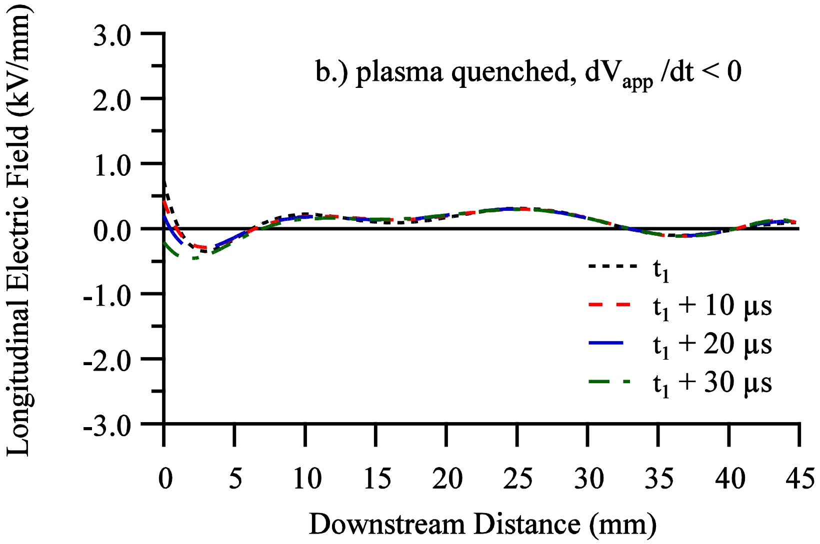

Figure 3.35: Electric field near the dielectric surface between t_1 and t_2 at 226 Torr.

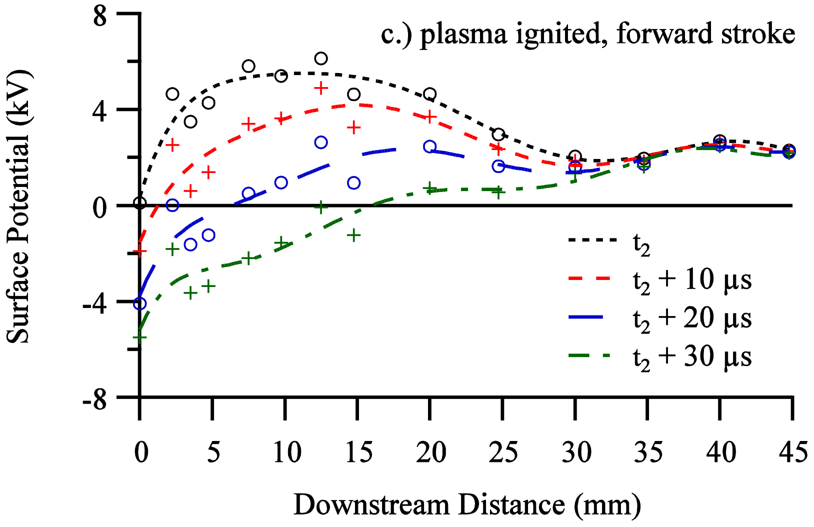

Figure 3.36: Potential on the surface of the dielectric between t$_2$ and t$_3$ at 226 Torr.

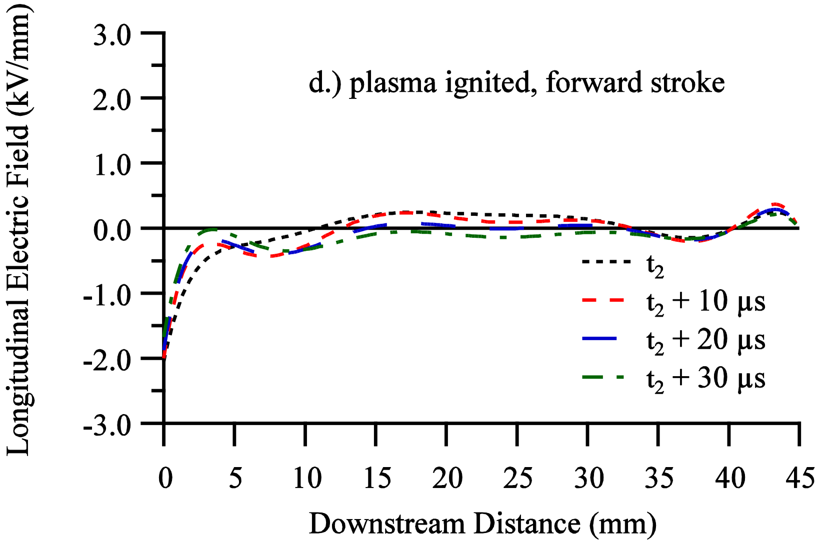

Figure 3.37: Electric field near the dielectric surface between t$_2$ and t$_3$ at 226 Torr.

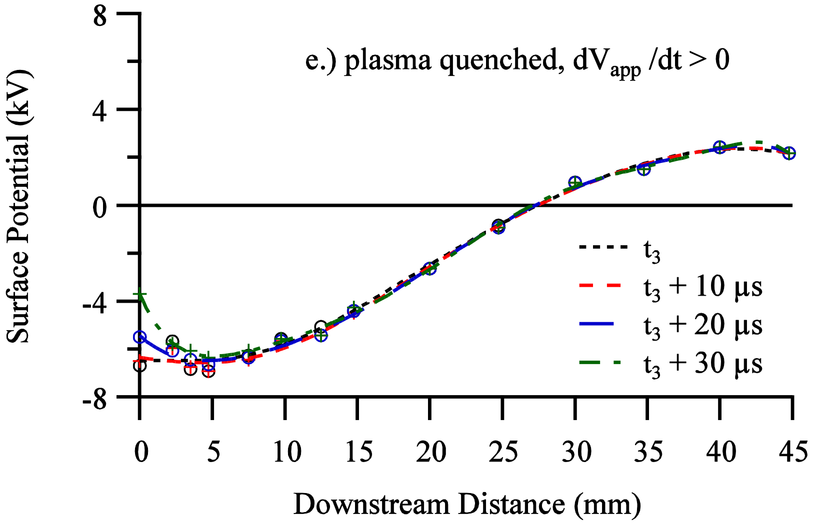

Figure 3.38: Potential on the surface of the dielectric between t_3 and t_4 at 226 Torr.

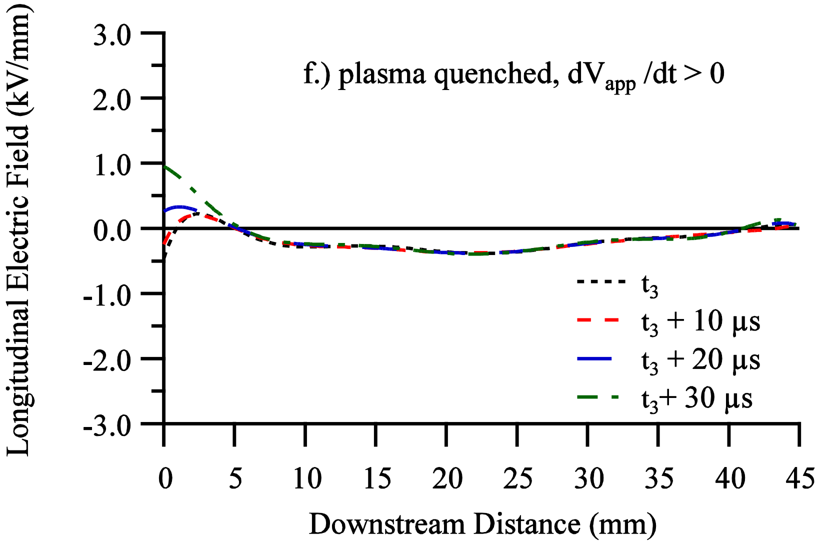

Figure 3.39: Electric field near the dielectric surface between t_3 and t_4 at 226 Torr.

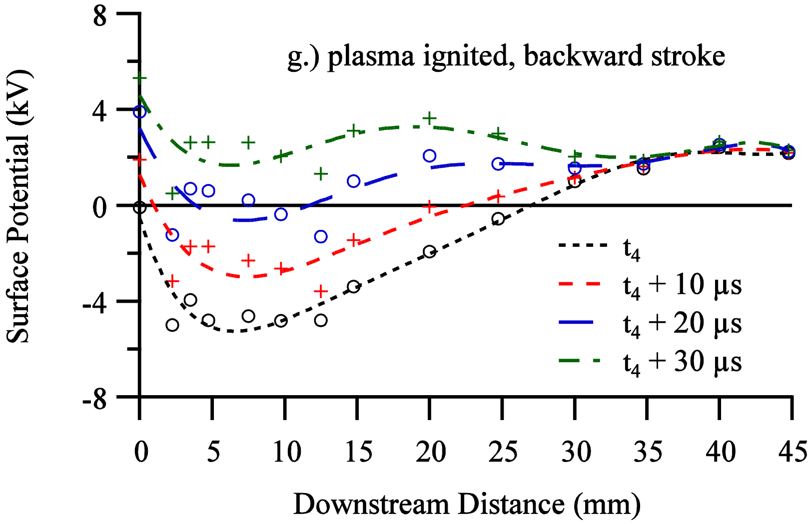

Figure 3.40: Potential on the surface of the dielectric after t_4 at 226 Torr.

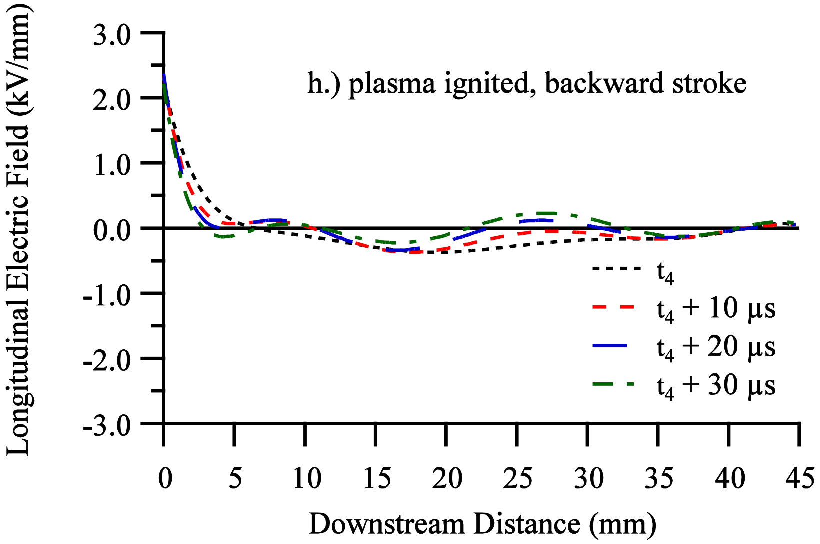

Figure 3.41: Electric field near the dielectric surface after t_4 at 226 Torr.

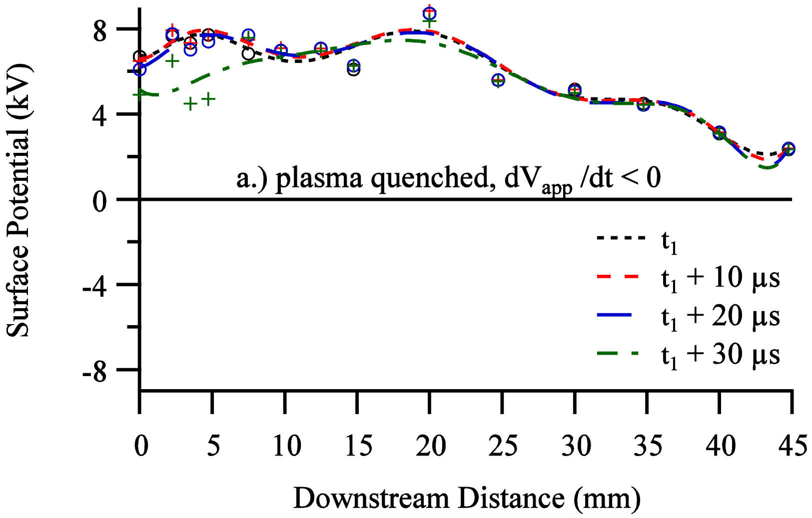

Figure 3.42: Potential on the surface of the dielectric between t_1 and t_2 at 171 Torr.

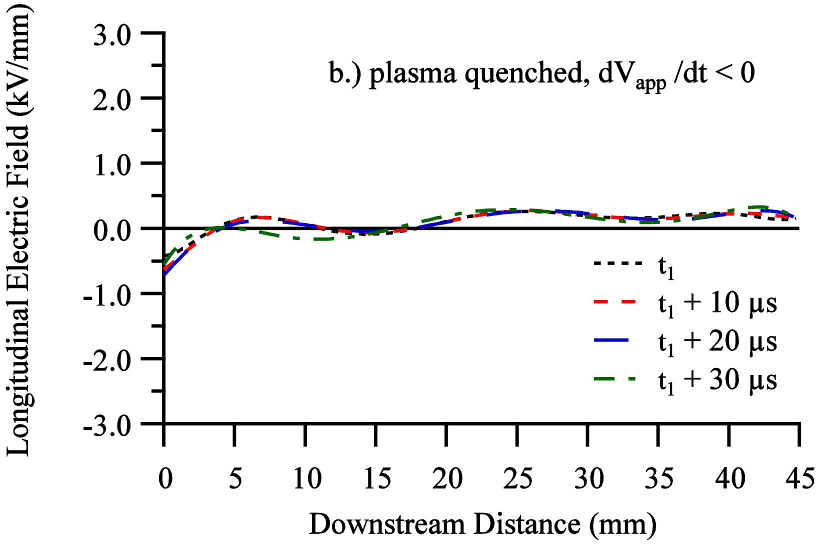

Figure 3.43: Electric field near the dielectric surface between t_1 and t_2 at 171 Torr.

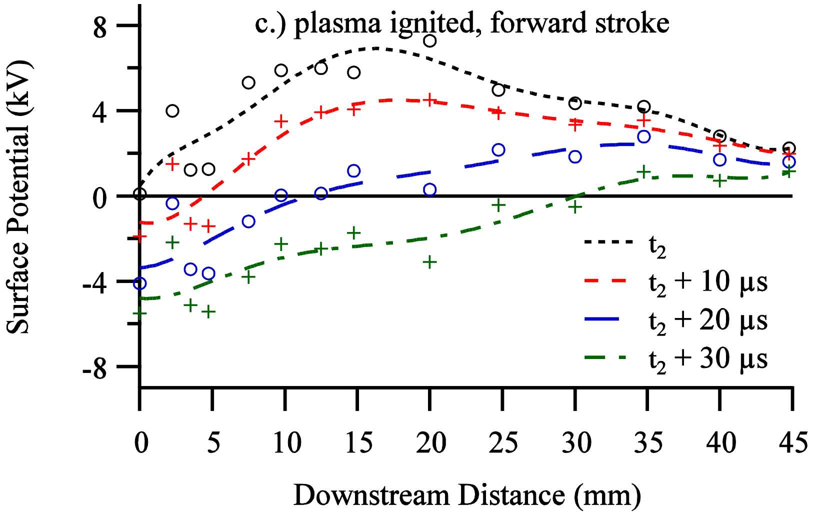

Figure 3.44: Potential on the surface of the dielectric between t_2 and t_3 at 171 Torr.

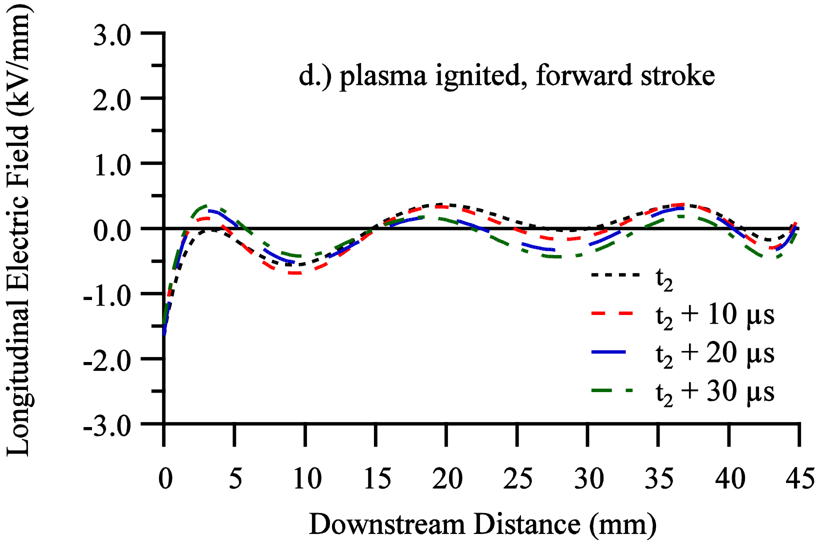

Figure 3.45: Electric field near the dielectric surface between t_2 and t_3 at 171 Torr.

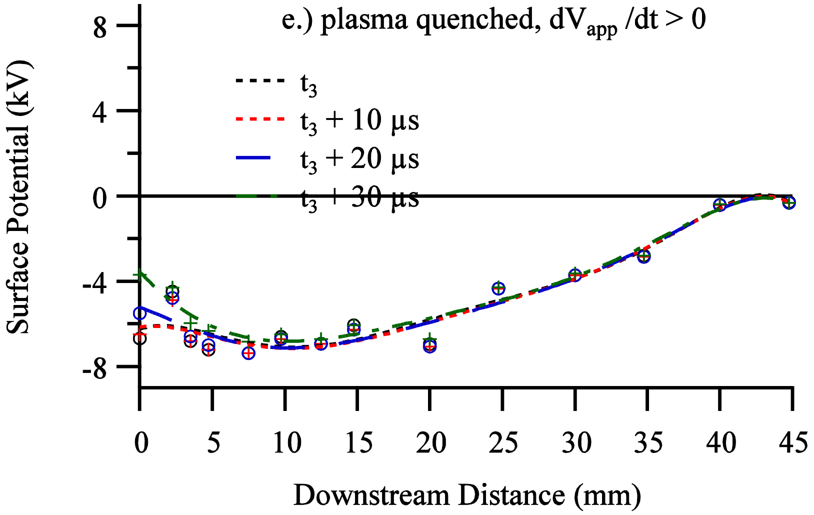

Figure 3.46: Potential on the surface of the dielectric between t_3 and t_4 at 171 Torr.

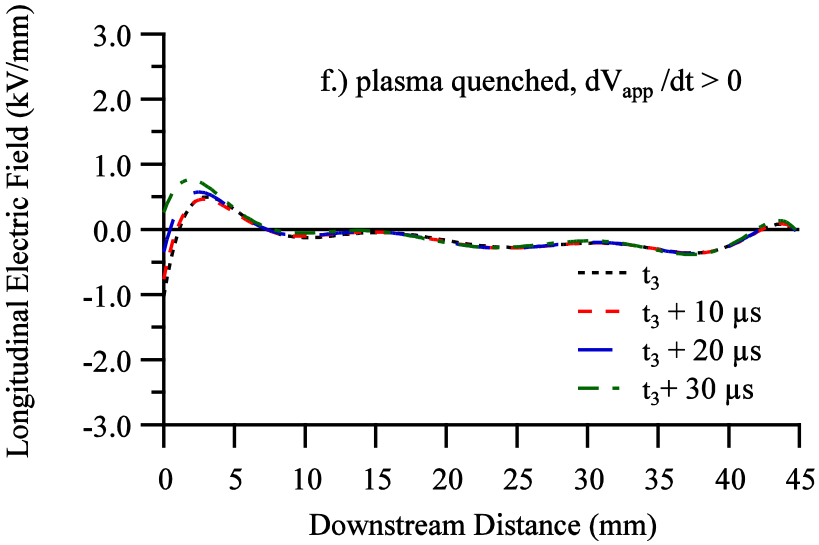

Figure 3.47: Electric field near the dielectric surface between t_3 and t_4 at 171 Torr.

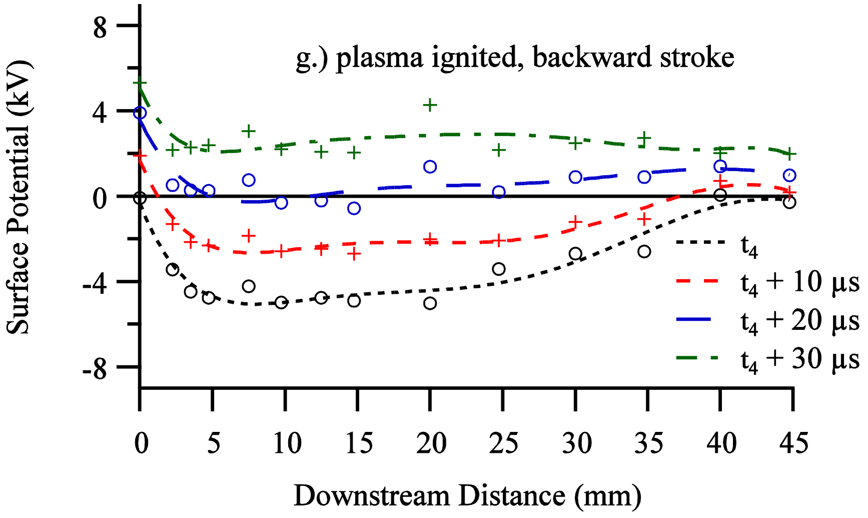

Figure 3.48: Potential on the surface of the dielectric after t_4 at 171 Torr.

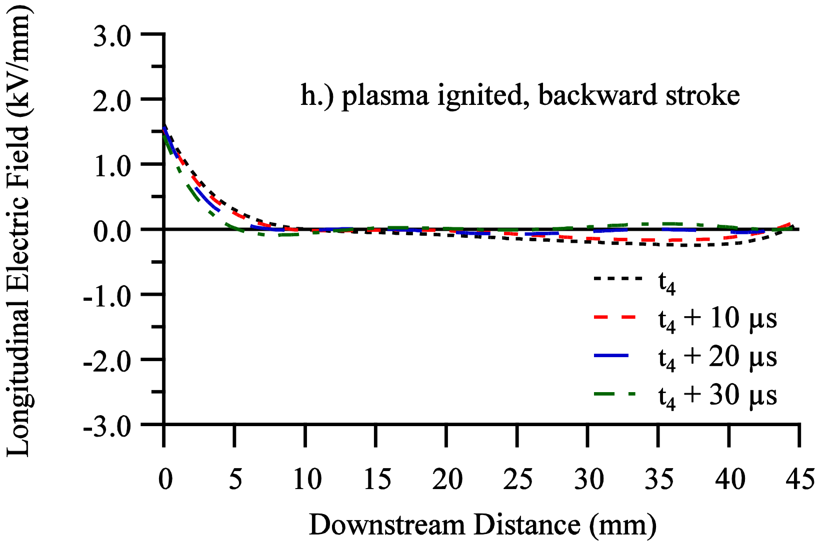

Figure 3.49: Electric field near the dielectric surface after t_4 at 171 Torr.

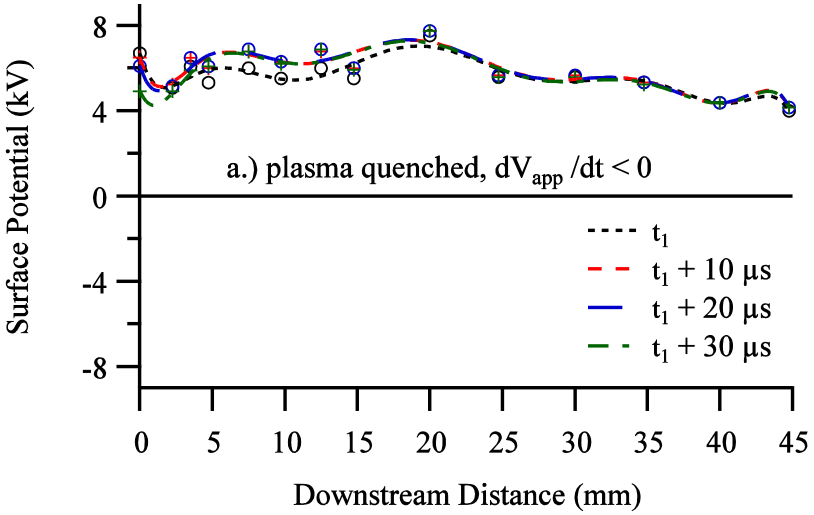

Figure 3.50: Potential on the surface of the dielectric between t_1 and t_2 at 88 Torr.

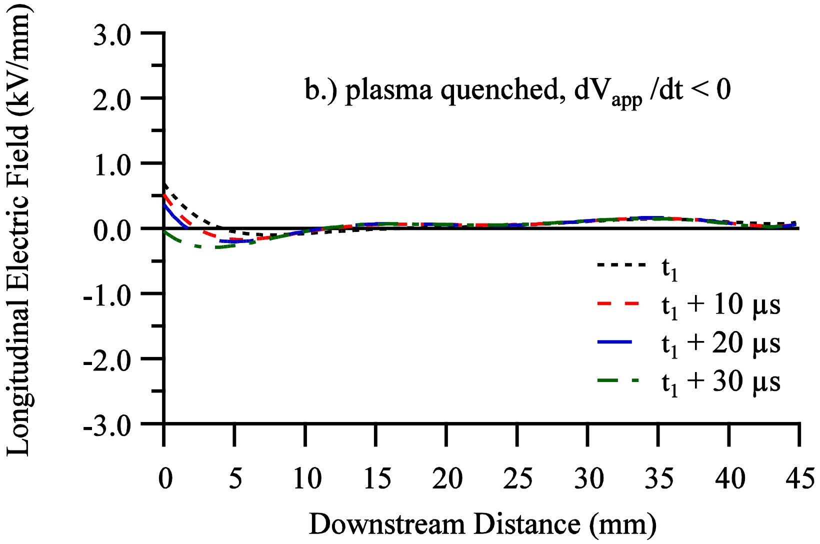

Figure 3.51: Electric field near the dielectric surface between t_1 and t_2 at 88 Torr.

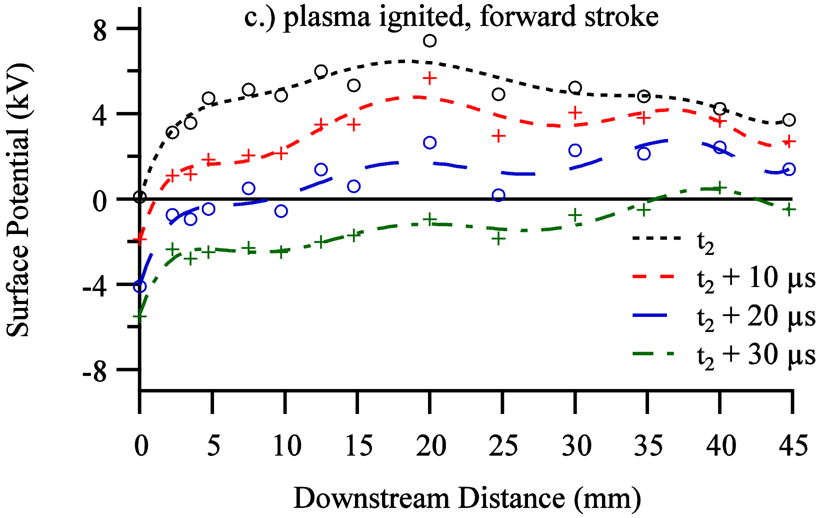

Figure 3.52: Potential on the surface of the dielectric between t_2 and t_3 at 88 Torr.

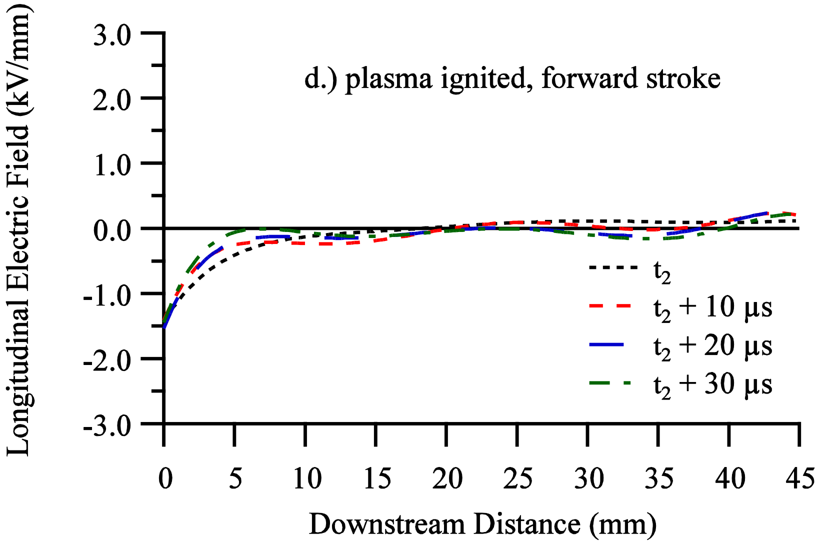

Figure 3.53: Electric field near the dielectric surface between t_2 and t_3 at 88 Torr.

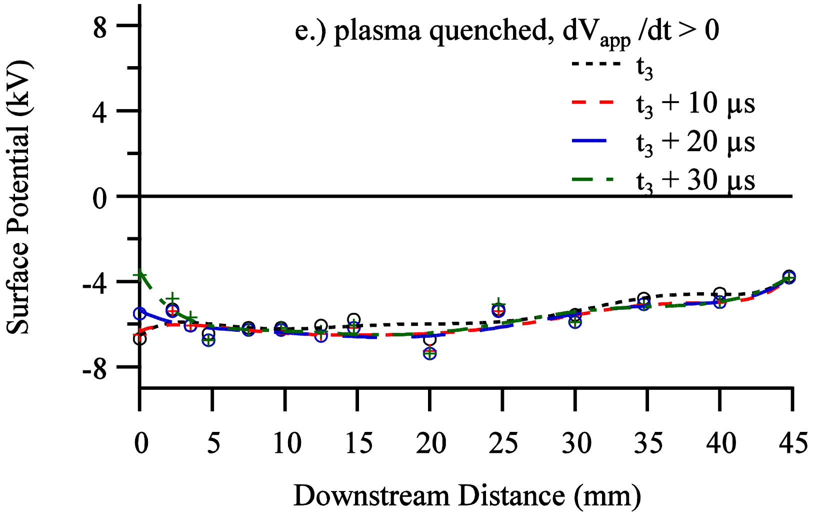

Figure 3.54: Potential on the surface of the dielectric between t_3 and t_4 at 88 Torr.

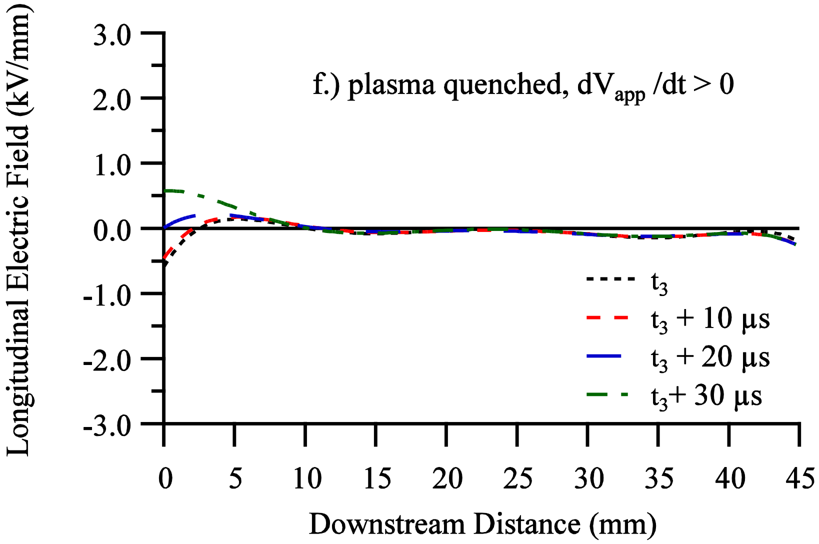

Figure 3.55: Electric field near the dielectric surface between t_3 and t_4 at 88 Torr.

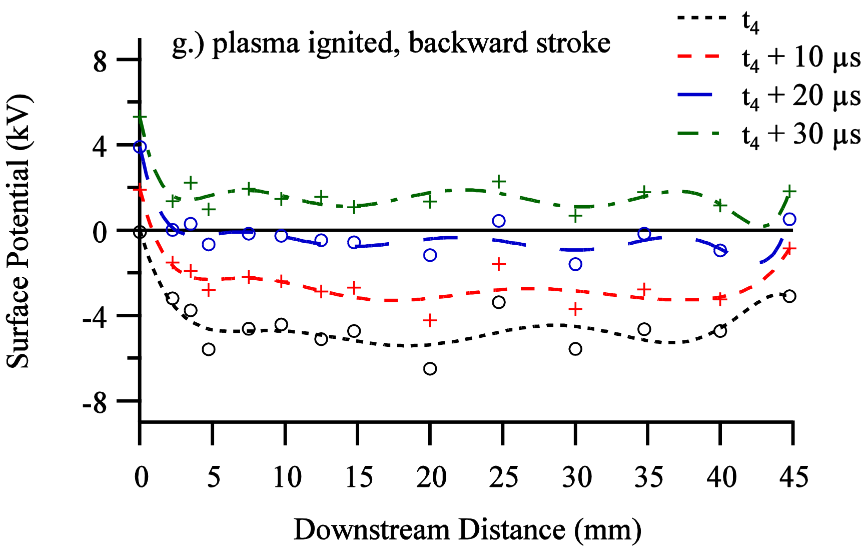

Figure 3.56: Potential on the surface of the dielectric after t_4 at 88 Torr.

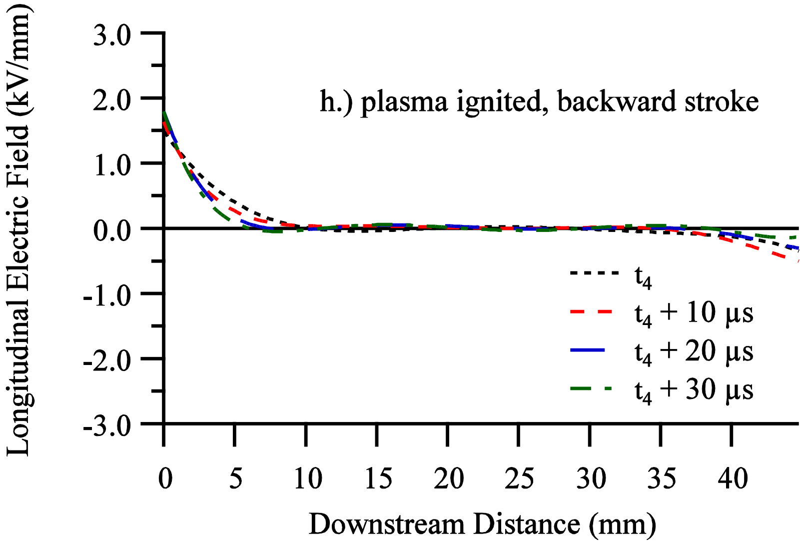

Figure 3.57: Electric field near the dielectric surface after t_4 at 88 Torr.

3.3. AVERAGE SURFACE POTENTIAL AND CHARGE TRANSFERRED

To better understand how the surface potential is distributed across the dielectric surface the average surface potential at each V-dot probe location was calculated. This is done by taking the average over a set number of applied AC signals (in this experiment, 4 periods) after equilibrium has been established. The results of this analysis are shown in Figure 3.58 - Figure 3.63 with error bars where appropriate. Similar conditions to those found in [24] are used in this work as the same material (Macor) was used as the dielectric material, as well as similar high voltage signals (13.4 kVpk-pk 5 kHz sine wave in [24]). Figure 3.58 shows that at 760 Torr the surface potential reaches a maximum value of 2.5 kV at a downstream location of 6.00 mm. Enloe et al. found that for similar conditions the largest surface potential is 1.67 kV at approximately 7.5 mm downstream [24]. At pressures of 429, 321, and 226 Torr the maximum average surface potential reaches a value of 3.0 kV at positions of x = 15, 20, and 40 mm, respectively. This shows that as the pressure decreases the region of largest surface potential moves farther downstream from the exposed electrode. During this same span of pressure drops, the width of the average surface potential also grows. At 760 Torr, there is a region of net positive potential from the exposed electrode edge 20.00 mm downstream. This region extends to 35 mm at 429 Torr until reaching the end of the V-dot probe array at 44.75 mm by 321 Torr. The entire dielectric surface maintains the net positive average surface potential at pressures of 171 Torr and 88 Torr.

Looking at Figure 3.62 and Figure 3.63, there is no peak surface potential downstream, indicating that the location of the peak surface potential has moved so far downstream that our V-dot probes are no longer able to capture it. Interestingly though, these plots do exhibit the smaller peak close to the exposed electrodes edge that begins to appear at 321 Torr. This local maximum is always located at approximately 2.5 mm downstream, regardless of the ambient pressure conditions. The amplitude of the maximum, however, is varied having a range of values of 0.75 kV, 0.45 kV, 0.6 kV, and 1.75 kV corresponding to the pressures from 321 Torr down to 88 Torr, respectively.

The results shown in Figure 3.64- Figure 3.69 depict how the average physical charge is deposited downstream as the ambient pressure is changed. Much like the average surface potential, the maximum charge transferred moves downstream as pressure decreases. In fact, the location for the peak charge transferred corresponds directly to the location of the peak average surface potential at a given pressure. This is to be expected as the contributions from the capacitive voltage division/polarization effects diminish far from the electrodes edge, meaning the only meaningful mechanism for building up surface potential is through physical charge deposition.

3.4. ION DENSITY

Assuming a linear relationship between light intensity and ion density, we use time-averaged photographs of the plasma to obtain a qualitative measurement of the ion density variation with pressure and downstream distance. A Canon PowerShot SX200IS with a shutter speed of 1/3 s and an ISO setting of 800 allows for time averaged photographs to be taken (such as those previously shown in Figure 3.3). These photos are converted to a gray scale value and normalized such that they can be compared directly to one another. In this way a value for light intensity, and subsequently ion density, can be obtained at all downstream locations. The results of this analysis can be seen in Figure 3.70. The highest density plasma is made at the exposed electrode edge at a pressure of

88 Torr. In fact, the densest region of plasma formation for a given pressure is always within 0.4 mm of the exposed electrode edge. The large spike next to the exposed electrode represents a region of intense microdischarges [14].

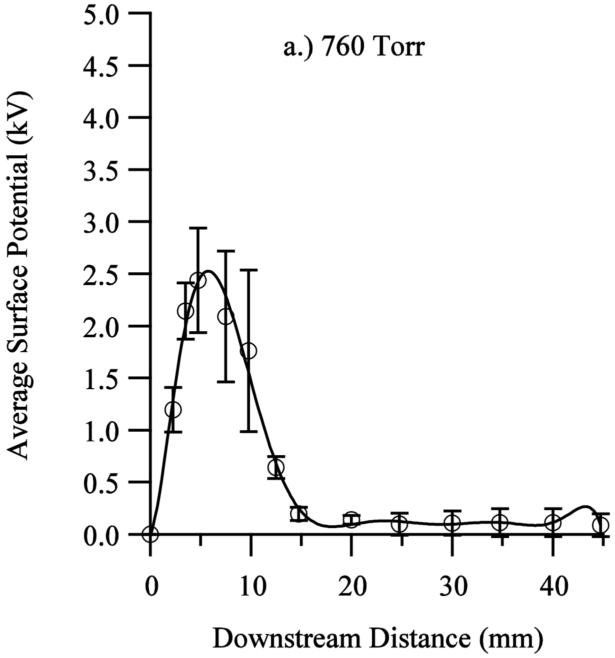

Figure 3.58: Average surface potential at 760 Torr.

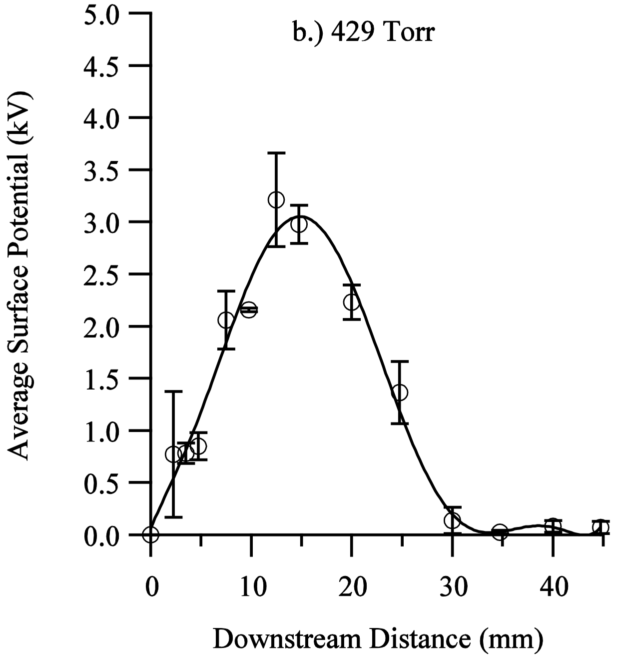

Figure 3.59: Average surface potential at 429 Torr.

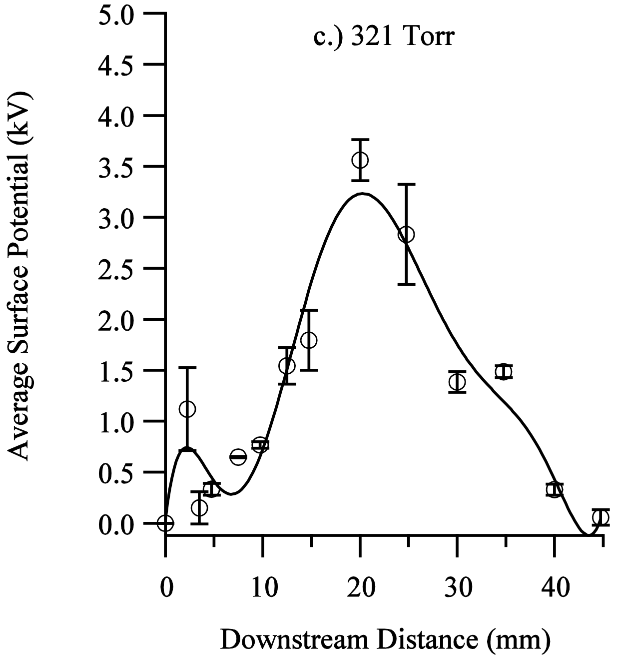

Figure 3.60: Average surface potential at 321 Torr.

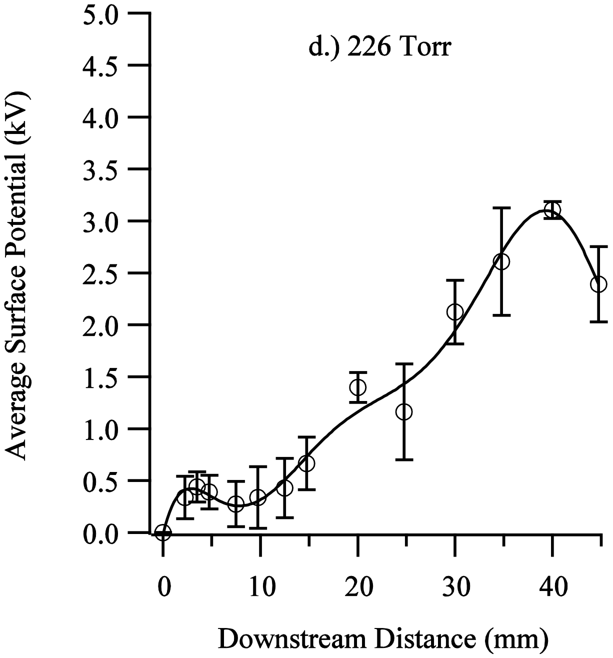

Figure 3.61: Average surface potential at 226 Torr.

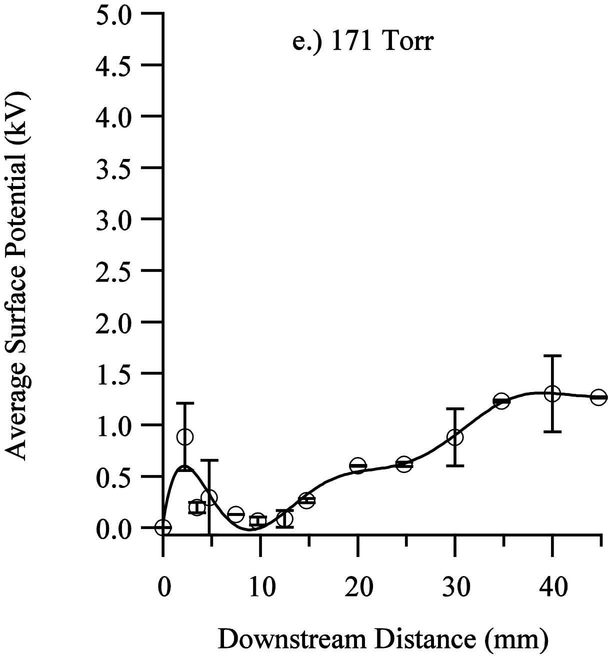

Figure 3.62: Average surface potential at 171 Torr.

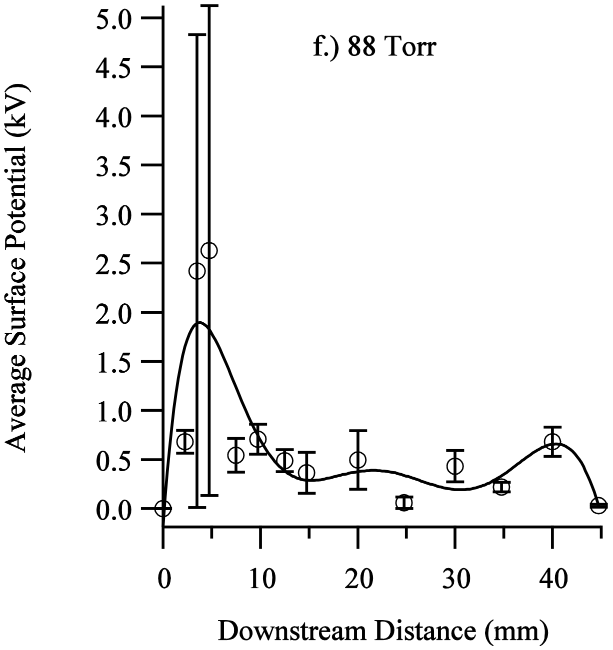

Figure 3.63: Average surface potential at 88 Torr.

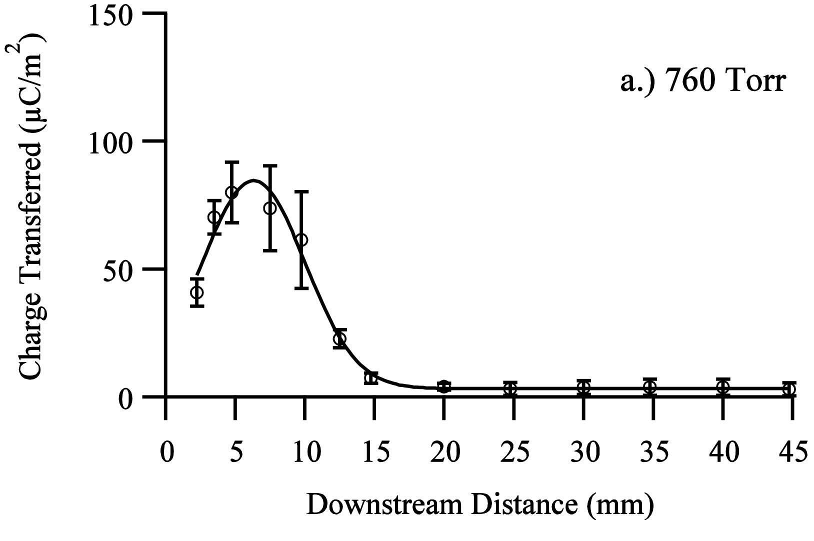

Figure 3.64: Average charge transferred at 760 Torr.

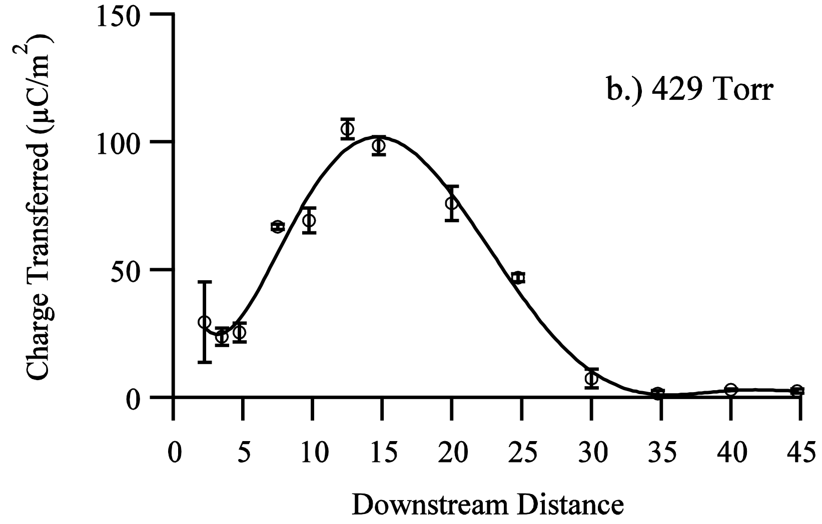

Figure 3.65: Average charge transferred at 429 Torr.

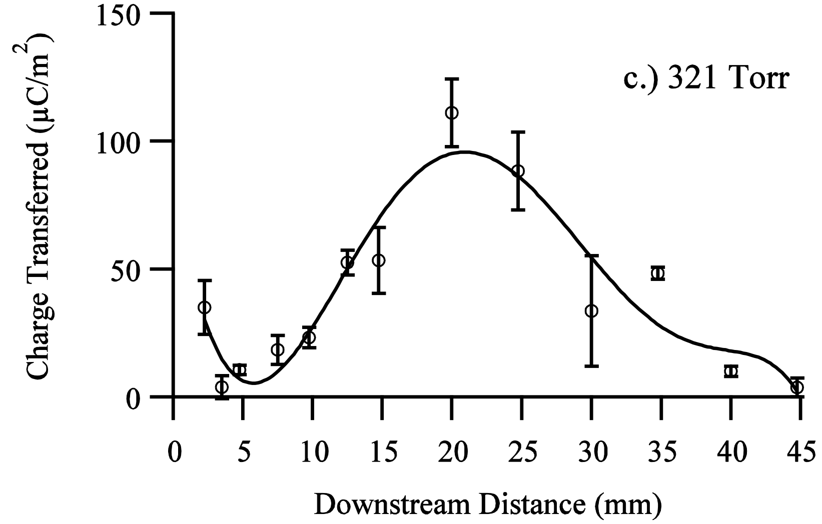

Figure 3.66: Average charge transferred at 321 Torr.

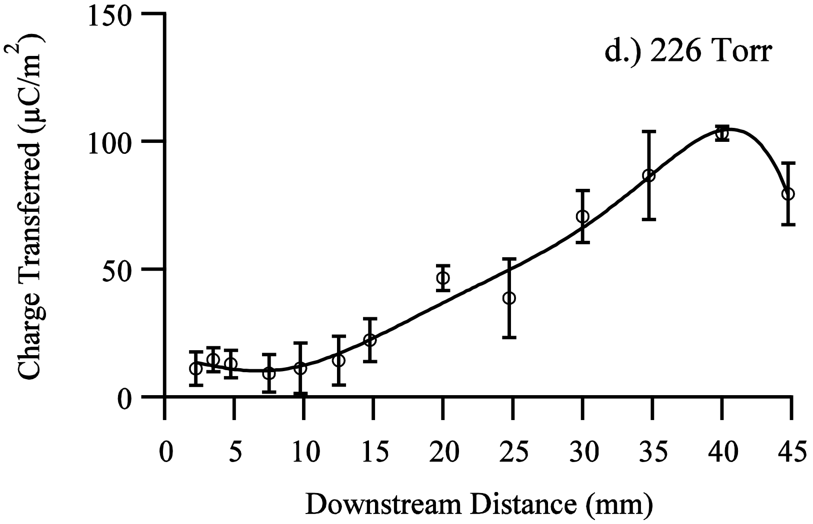

Figure 3.67: Average charge transferred at 226 Torr.

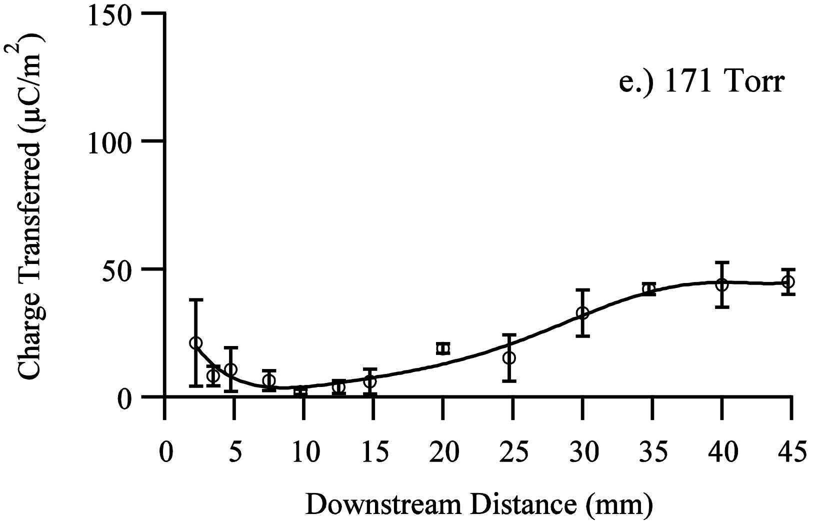

Figure 3.68: Average charge transferred at 171 Torr.

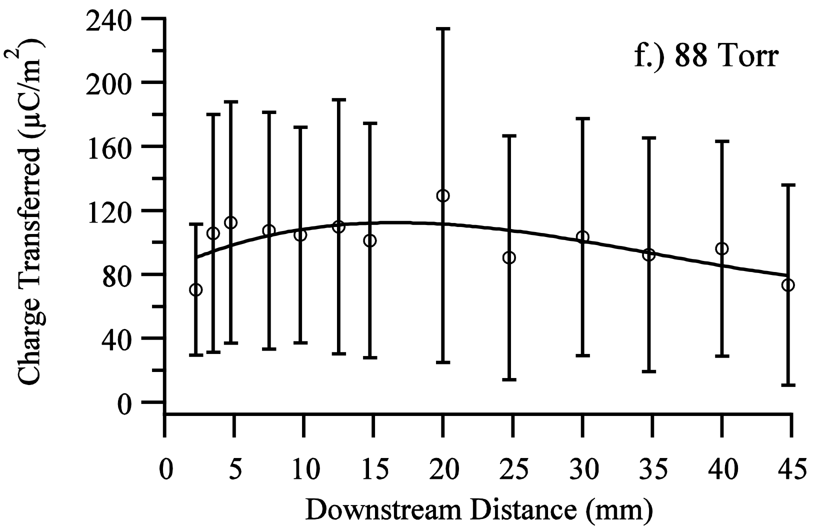

Figure 3.69: Average charge transferred at 88 Torr.

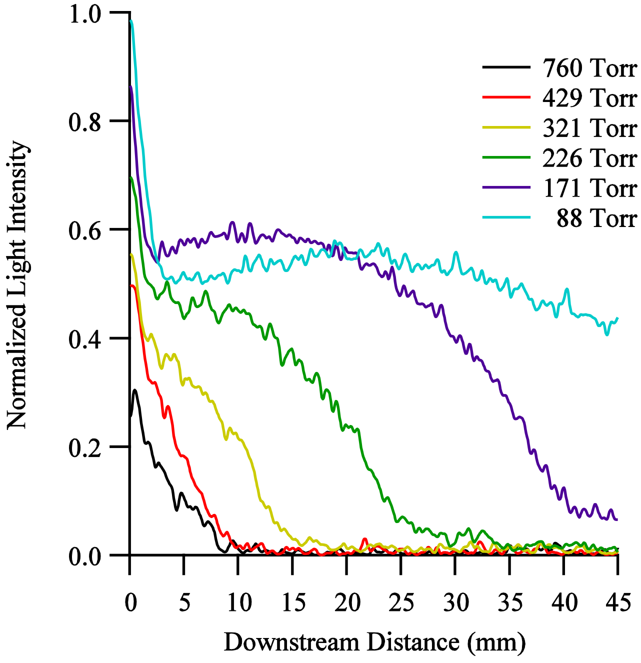

Figure 3.70: Calculating the normalized light intensity allows for the determination of a qualitative measurement for the ion density at any downstream location.

4. DISCUSSION

The overall trends and effects that ambient pressure has on the surface potential of the dielectric, generated electric field, and average force production of the plasma actuator are discussed here.

4.1. SURFACE POTENTIAL AND CHARGE BUILD-UP

As shown in Figure 4.1, the maximum charge transferred moves downstream as pressure decreases in similar fashion to the average surface potential. Only those pressures down to 226 Torr are plotted due to the fact that at lower pressures the maximum average surface potential has moved past our farthest V-dot probe. The polarization effect that contributes to the overall surface potential is mainly seen at downstream distances of 2.5 mm or less, where the electric field is the strongest. This means that the dominant mechanism for building surface potential at downstream distances that are far from the leading edge of the exposed electrode is physical charge deposition. Finally, the maximum average surface potential and charge transferred are inversely proportional to the pressure.

4.2. LOCATION OF PLASMA PRODUCTION

Body force produced by a plasma actuator is directly proportional to the number of plasma ions present and the strength of the electric field where those ions are produced (Eq. (1)). By integrating each curve in Figure 3.70, it is possible to qualitatively determine the quantity of plasma present for a given operating pressure. The normalized results are shown in Figure 4.2. As is shown, there is 20 times more plasma produced at 88 Torr than at 760 Torr. This increase is inversely proportional to the ambient pressure. It is also interesting to examine the electric field in the region where the plasma is created. By combining the plasma extent measurements (Figure 3.3) with the electric field data presented in Figure 3.10-Figure 3.57, it is possible to determine the fraction of the plasma extent with no electric field. The results of this analysis are also shown in Figure 4.2.

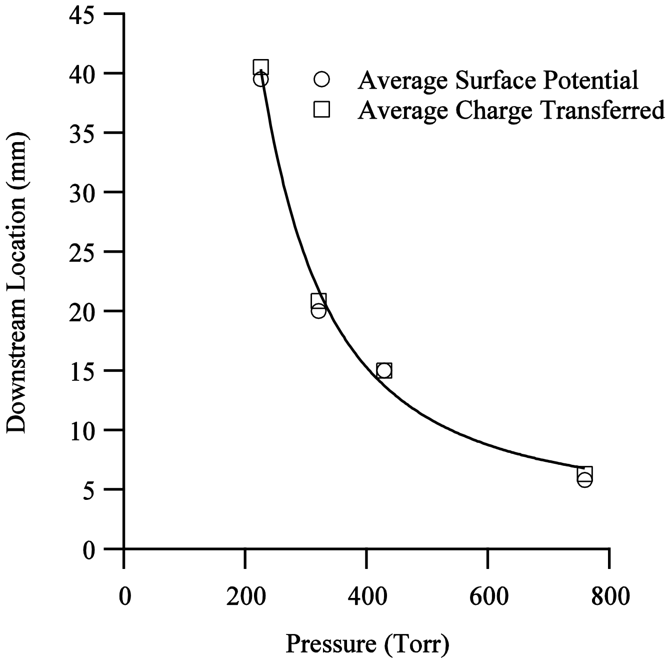

Figure 4.1: The location of the maximum average surface potential and charge transferred moves downstream as pressure decreases in a similar non-linear fashion as Figure 3.2.

From 760 to 321 Torr all plasma is created in a region where the electric field has some non-zero magnitude. As pressure is decreased further this trend changes significantly. For the tested pressures of 226, 171, and 88 Torr, 38, 74, and 88 percent of the plasma is created in regions of approximately zero electric field, respectively. While there is 20 times more plasma present at 88 Torr than at 760 Torr, 88 percent of the plasma is in a region where there is no electric field present to accelerate it.

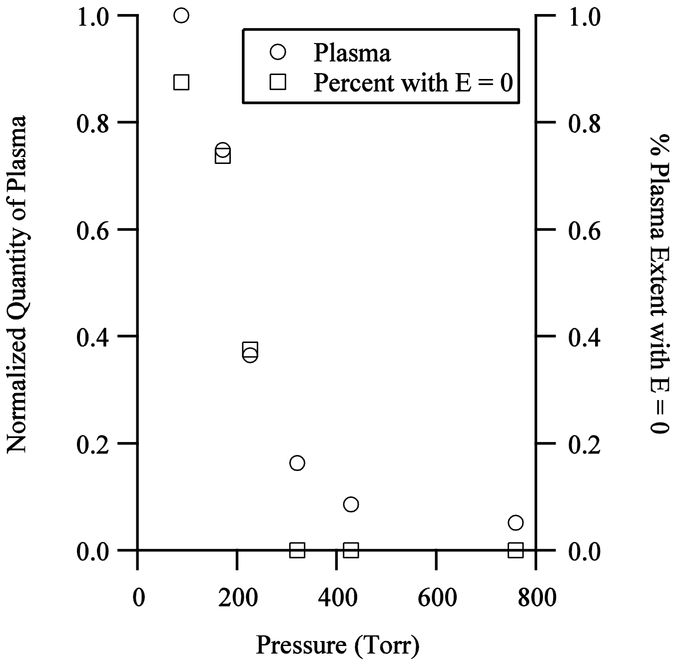

Figure 4.2: As pressure decreases a larger percentage of plasma is formed where the electric field is approximately zero.

4.3. QUALITATIVE FORCE TRENDS

With the data presented in this paper it is possible to calculate the qualitative average body force that the plasma actuator produces. In order to calculate the force produced by our plasma actuator the electric field results are averaged with respect to time. A spatial average of the combined electric field and ion density is performed to obtained the qualitative time-average force. This is done in order to multiply the spatial electric field data with the qualitative spatial ion density measurements. These calculations are compared with measurements presented in [19] and recreated in Figure 4.3. This work is used for comparison due to similar operating parameters (shape, frequency, and amplitude of the sine wave) and the number of pressures that were tested. A direct comparison cannot be made between this work and [19] due to differences in how force is calculated/measured, however, a similar qualitative trend is still evident between the two experiments. Looking at Figure 4.3 it is evident that there is a local maximum force produced around 600 Torr for an exposed electrode thickness of 0.2 mm. While this work cannot conclusively confirm this, it is possible to say that the force does increase between 760 and 429 Torr before beginning to decrease. Overall, the two separate works show good agreement as the pressure is decreased, with an initial increase in force before decreasing and trending to zero.

It is worthwhile to now compare the calculated force for the current plasma actuator and the power consumption. Looking again at Figure 3.2 and comparing with the force production shown in Figure 4.3 it is possible to make some comments about how the power consumed is being used by the plasma actuator. Looking at the region of pressures between 226 and 88 Torr and the corresponding power consumption at those pressures we see that although the power consumption is increasing, the force production is decreasing. This is further evidence that as pressure is decreased, more power is being used in processes not related to force production. Since the mechanism for force production comes from the momentum coupling that occurs due to the acceleration of the plasma and since the electric field (the accelerating source of the ions) has been measured and calculated to be zero far from the exposed electrode edge where large amounts of plasma are formed, it is now possible to say that the increased power consumption is for generating plasma and not accelerating it.

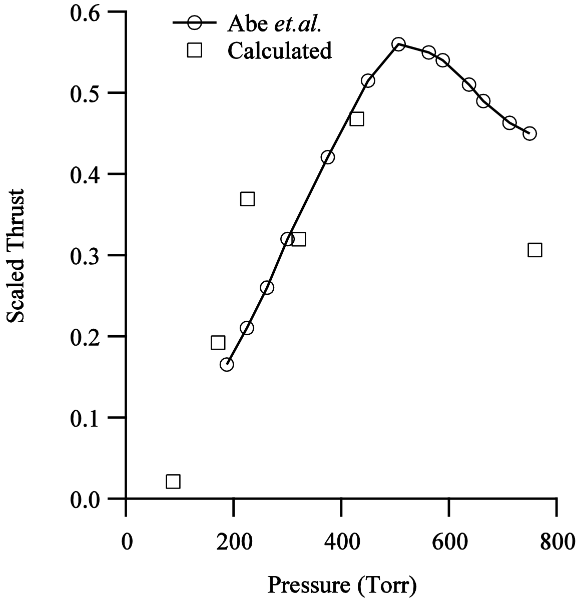

Figure 4.3: The space and time average force for this work shows similar trends to that of the force measured by Abe et al. [19].

5. **CONCLUSION**

In this paper measurements done with an array of capacitive V-dot probes of the potential on the dielectric surface have been presented. While the surface potential is spread out across the dielectric surface as pressure decreases, the electric field only exhibits a slight decrease in magnitude close to the exposed electrode edge. As pressure is decreased from 760 to 88 Torr up to 20 times more plasma becomes available for acceleration, and thus force production. At lower pressures, however, up to 88 percent of the plasma is created in a region where there is an effective electric field strength of zero. Because the acceleration of the plasma ions is the means for force production it follows that this is why force production trends to zero as pressure is decreased. The average force calculations further show this trend with an initial increase in force production before trending to zero. This suggests that there is an optimum amount of plasma, and thus an optimum pressure, to operate the plasma actuator at in order to produce the maximum amount of force. These trends are in good agreement with those presented in the literature [19]. By looking at the plasma extent, power consumption, and force production at a given pressure it is possible to conclude that at low pressures (226 Torr and below) more power is going into creating plasma than accelerating it.

Future work on SDBD plasma actuators operating at high altitude should focus on resolving the spatiotemporal evolution of the force produced. Using a high speed camera with an appropriate sensor would do well to temporally resolve the ion density which could then be multiplied with the temporally resolved electric field calculated in this paper.

APPENDIX A.

MISCELLANEOUS PLOTS

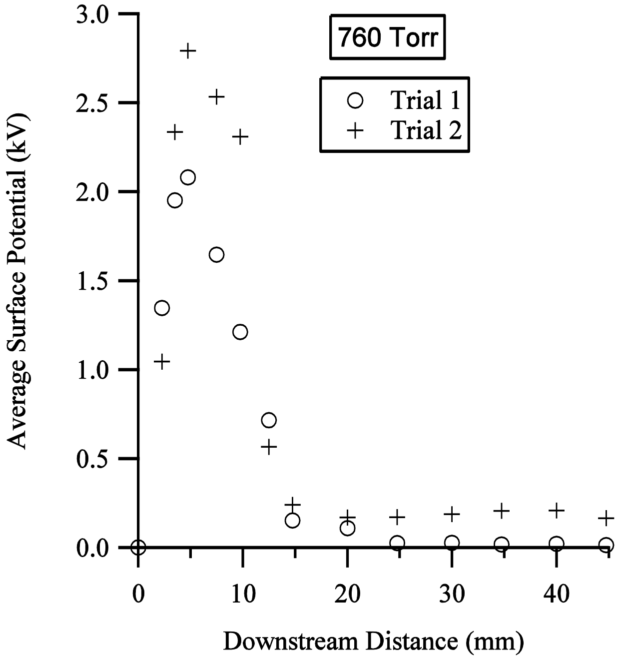

Figure A.1: Average surface potential for each individual trial ran at 760 Torr.

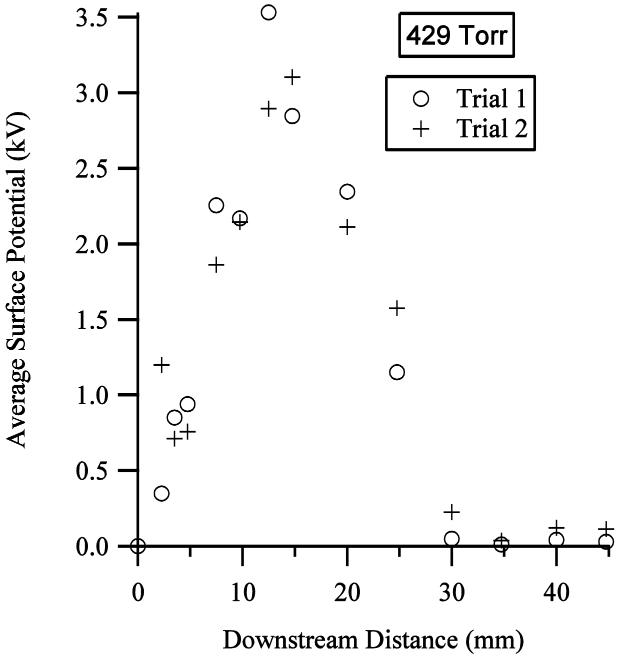

Figure A.2: Average surface potential for each individual trial ran at 429 Torr.

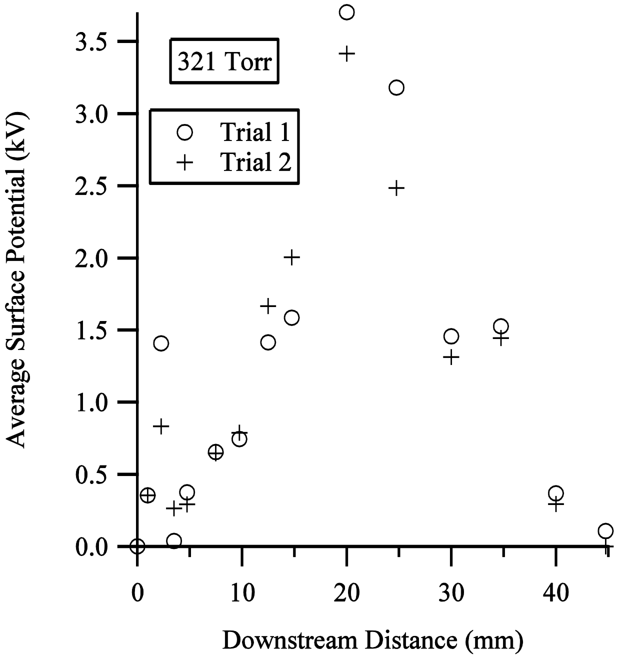

Figure A.3: Average surface potential for each individual trial ran at 321 Torr.

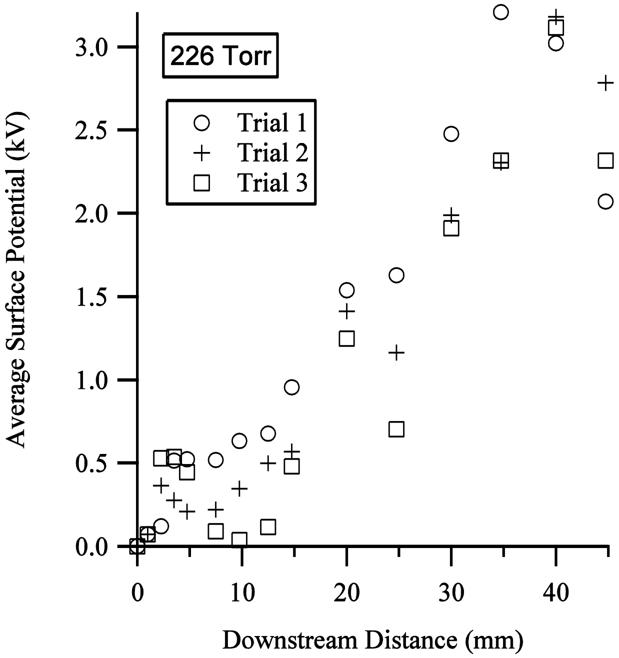

Figure A.4: Average surface potential for each individual trial ran at 226 Torr.

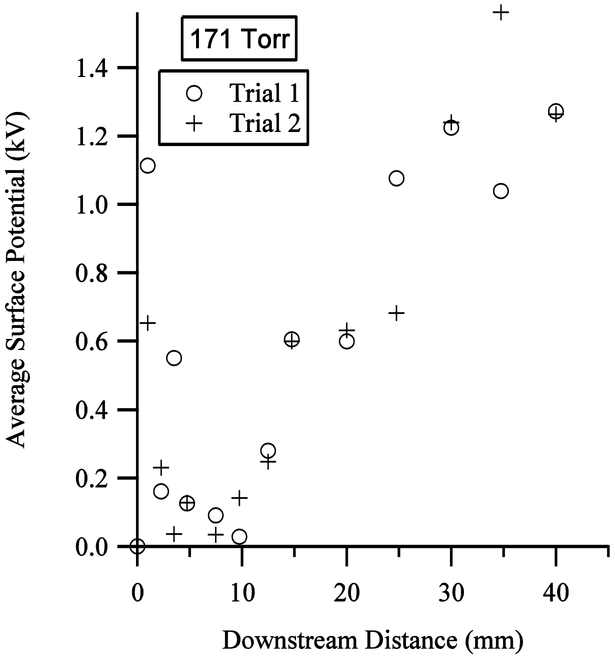

Figure A.5: Average surface potential for each individual trial ran at 171 Torr.

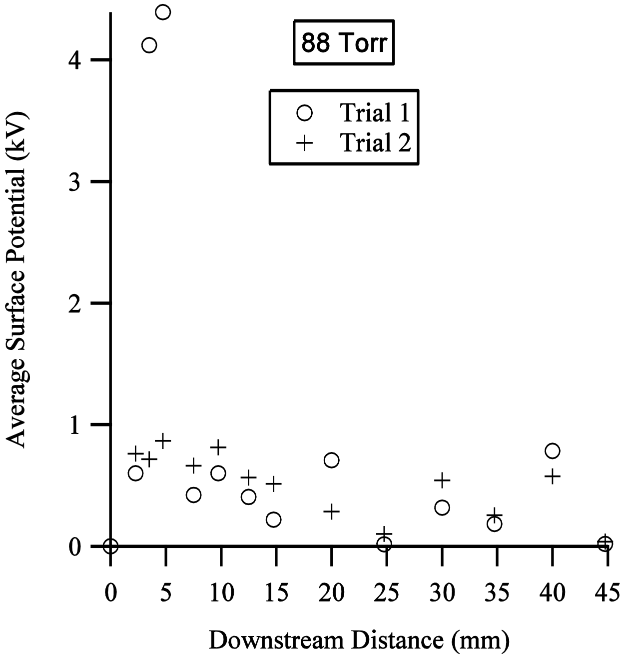

Figure A.6: Average surface potential for each individual trial ran at 88 Torr.

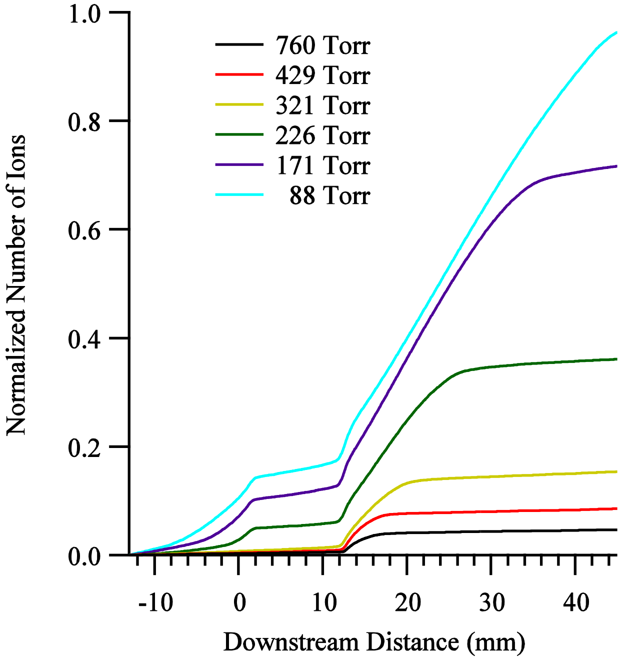

Figure A.7: Plot of the normalized number of ions

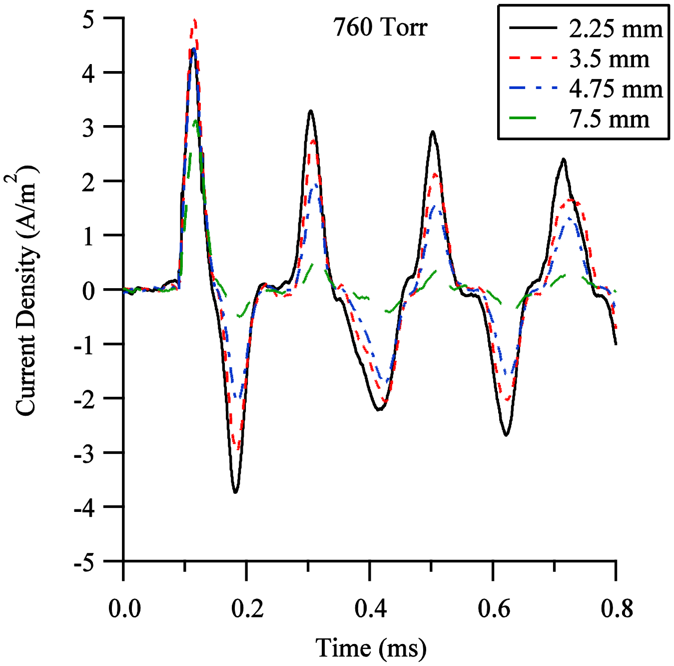

Figure A.8: Current density for probes 2-5 at 760 Torr.

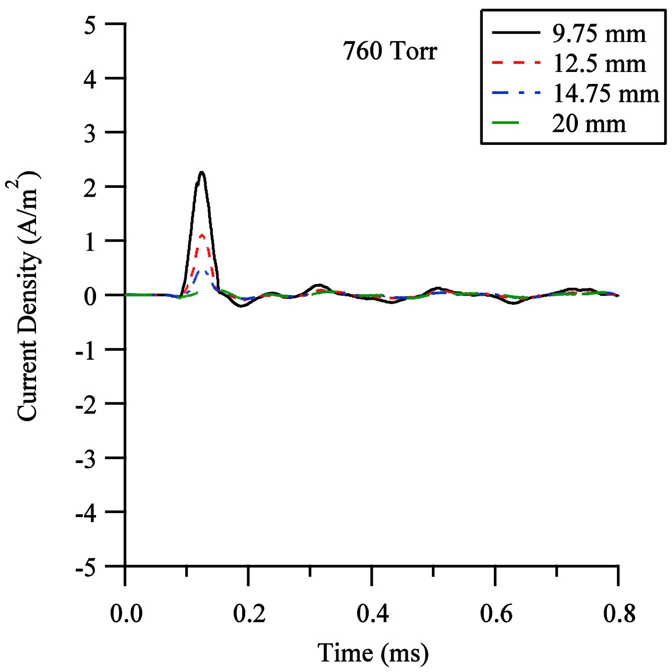

Figure A.9: Current density for probes 6-9 at 760 Torr.

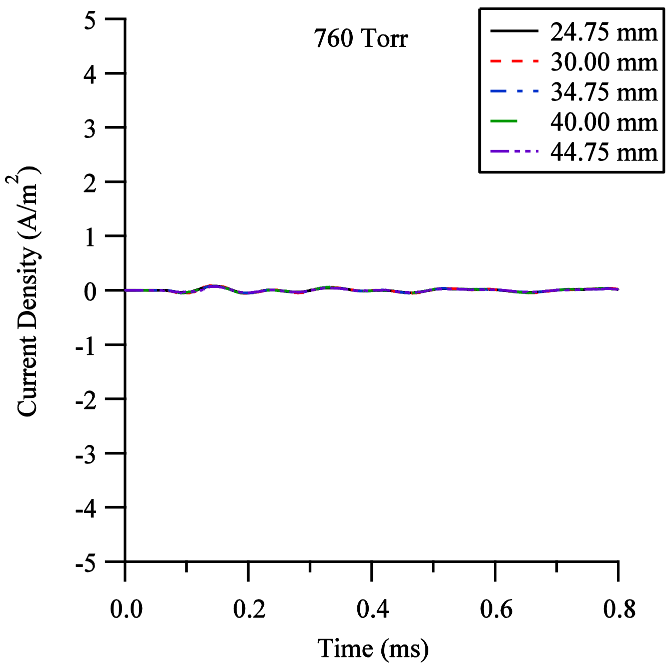

Figure A.10: Current density for probes 10-14 at 760 Torr.

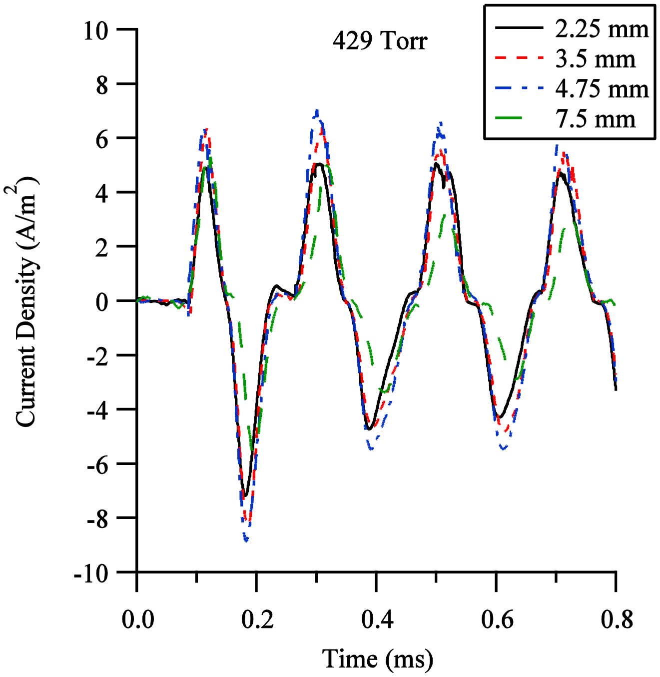

Figure A.11: Current density for probes 2-5 at 429 Torr.

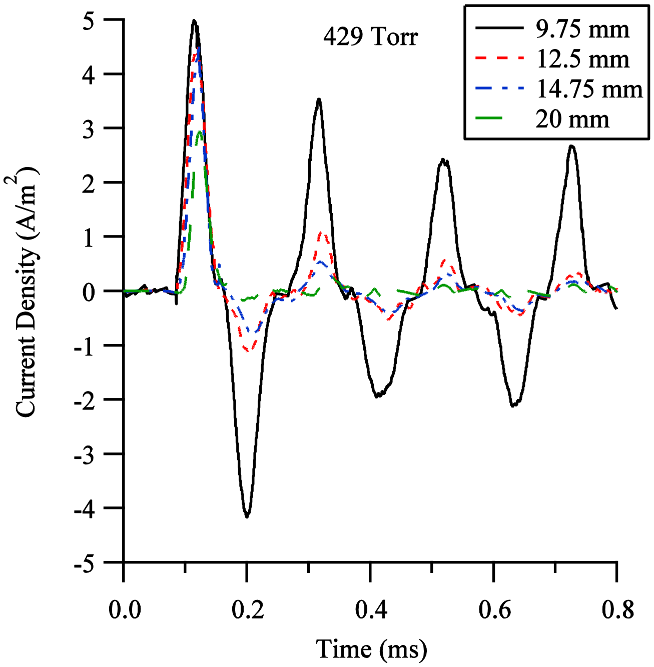

Figure A.12: Current density for probes 6-9 at 429 Torr.

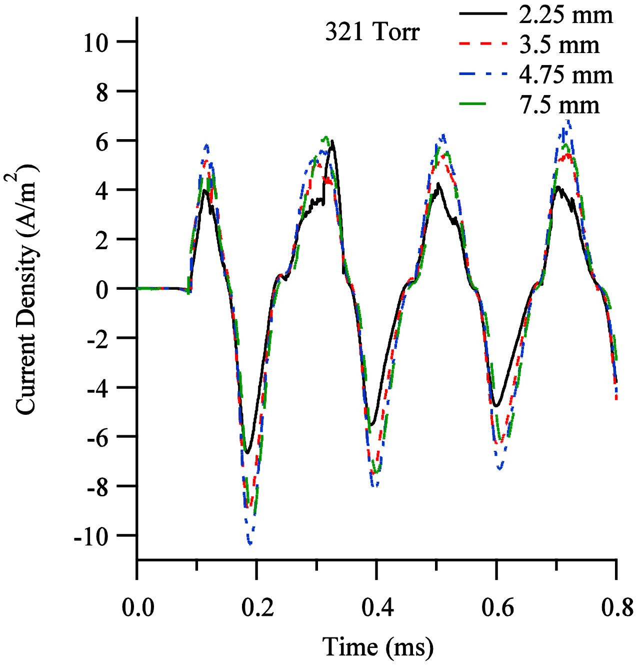

Figure A.13: Current density for probes 2-5 at 321 Torr.

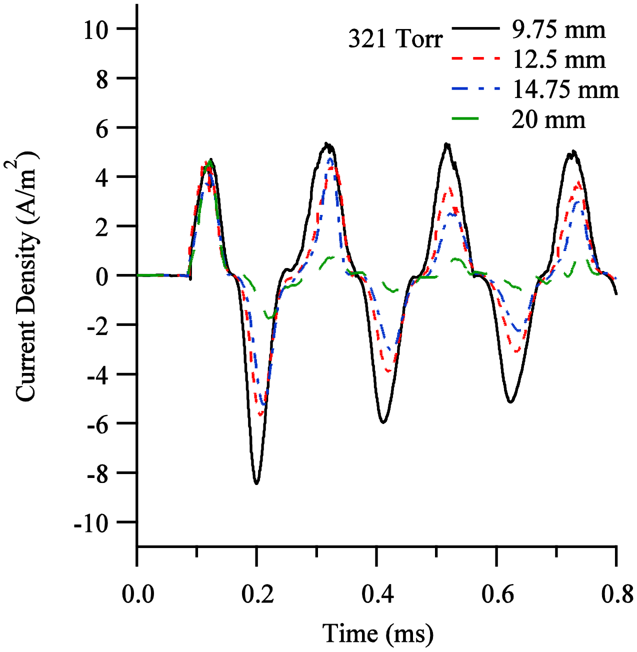

Figure A.14: Current density for probes 6-9 at 321 Torr.

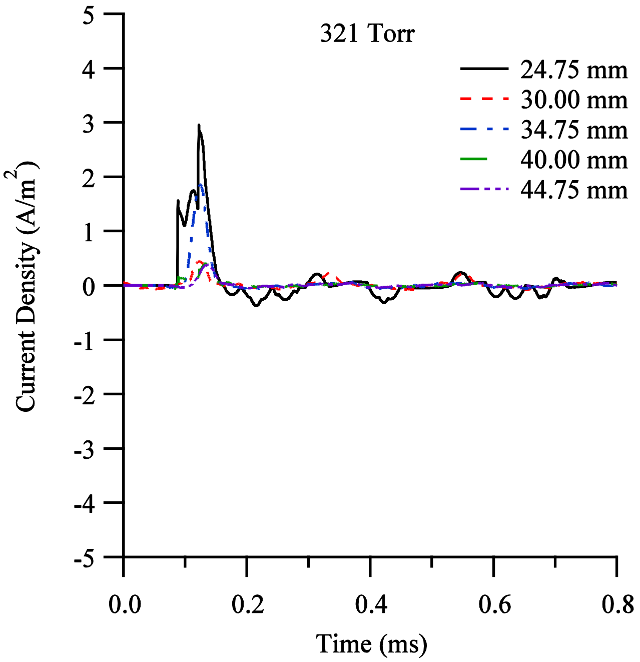

Figure A.15: Current density for probes 10-14 at 321 Torr.

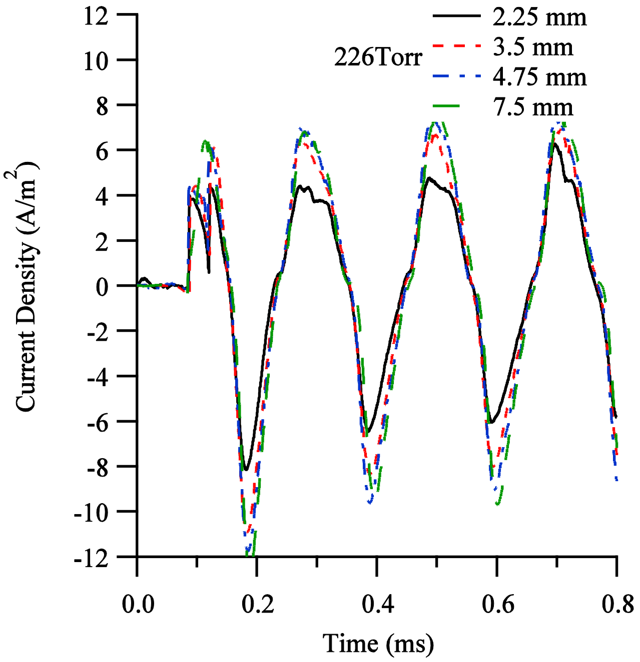

Figure A.16: Current density for probes 2-5 at 226 Torr.

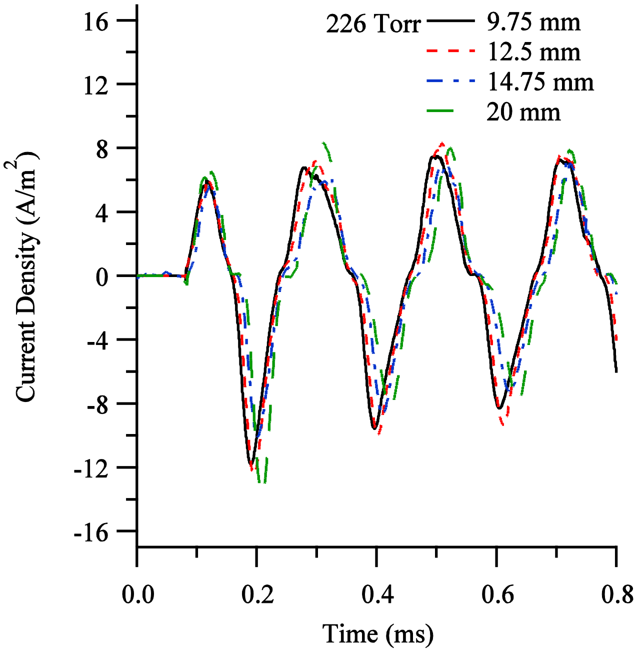

Figure A.17: Current density for probes 6-9 at 226 Torr.

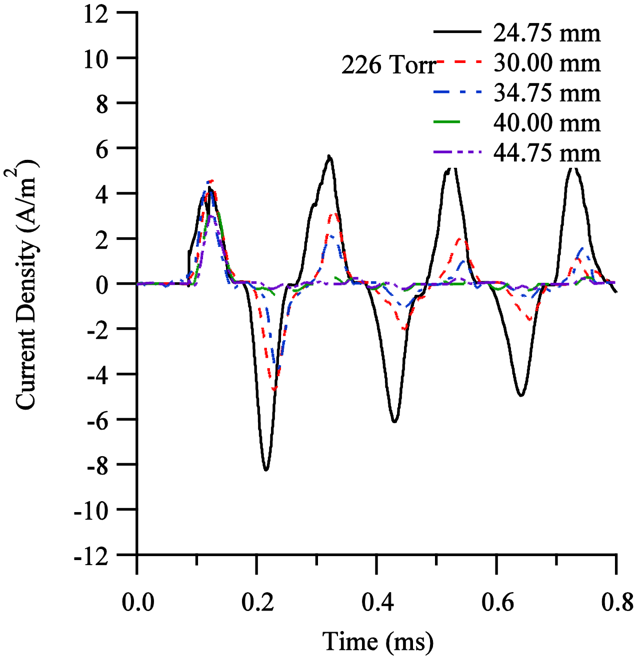

Figure A.18: Current density for probes 10-14 at 226 Torr.

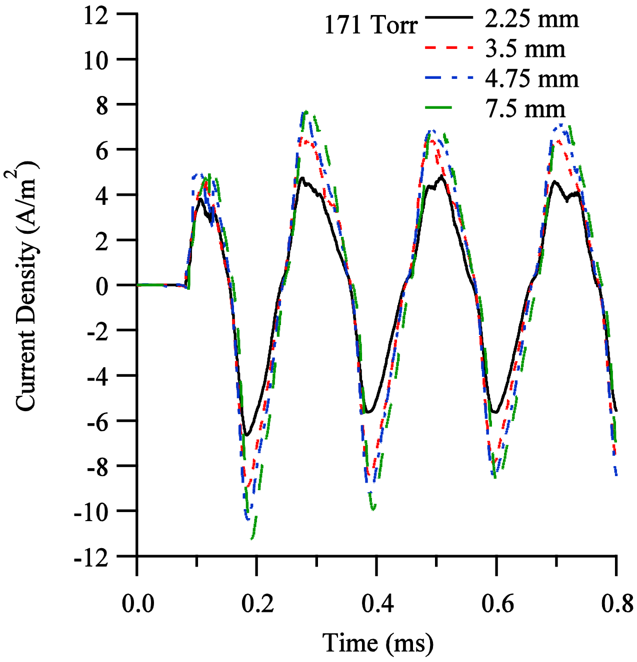

Figure A.19: Current density for probes 2-5 at 171 Torr.

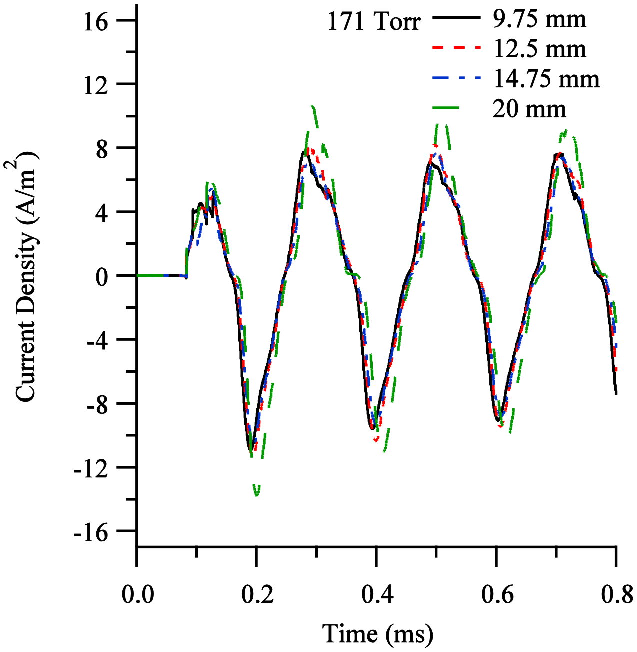

Figure A.20: Current density for probes 6-9 at 171 Torr.

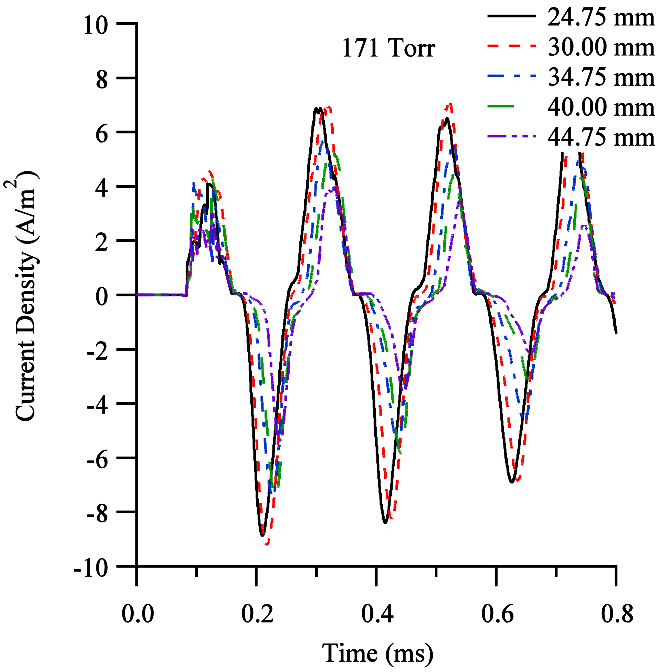

Figure A.21: Current density for probes 10-14 at 171 Torr.

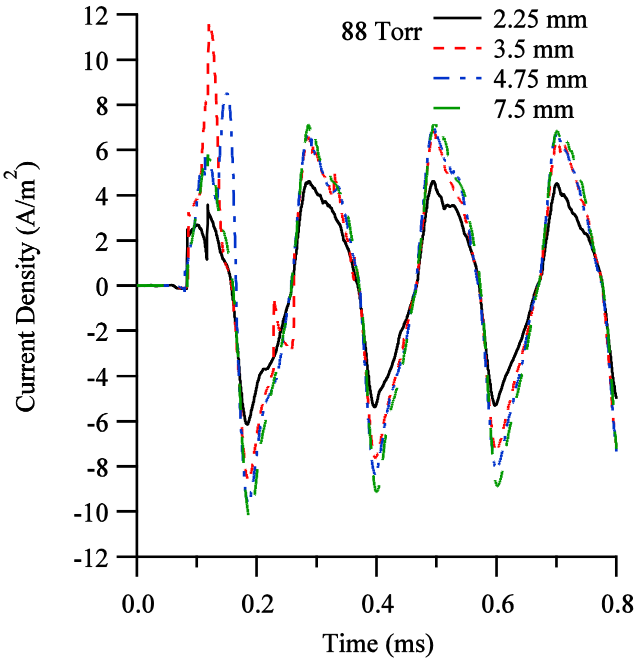

Figure A.22: Current density for probes 10-14 at 88 Torr.

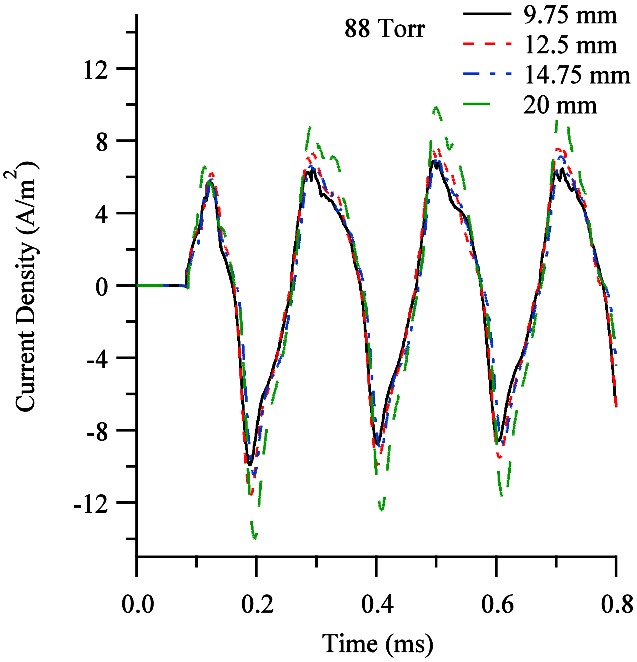

Figure A.23: Current density for probes 6-9 at 88 Torr.

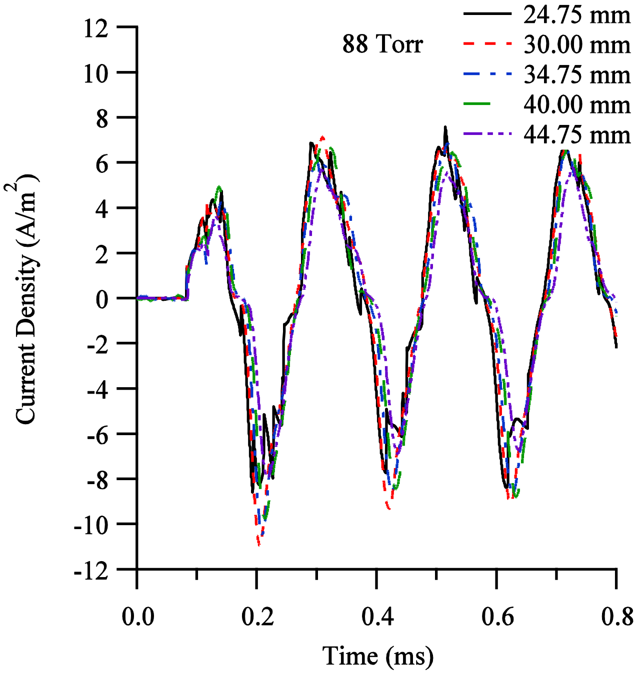

Figure A.24: Current density for probes 10-14 at 88 Torr.

APPENDIX B.

DETAILED TROUBLESHOOTING OF EXPERIMENTAL SETUP

In this appendix a detailed guide to troubleshooting and setting up the high altitude plasma actuator experiment is given.

B.1. HIGH VOLTAGE PASSTHROUGH AND HIGH VOLTAGE WIRE

The high voltage pass-through and high voltage wire shown in Figure B.1 are used in this experiment for a number of reasons. The first reason is due to arcing. At standard atmospheric pressure a lower gauge, less insulated wire can be used, however, when operating at lower pressures it is recommended a wire such as the E76475 from Thermal Wire and Cable Corp. be used. This wire is rated to 40 kV DC and helps to reduce the chance of arcing at low pressures. If a thinner, lower voltage rating wire is used plasma can form within the wire itself.

The high voltage pass-through used on the bell jar is a lab made pass-through. Commercial pass-throughs are available, however, they do not provide for enough insulation against arcing between the pass-through itself and the vacuum chamber. Because of this the high voltage wire is run through the pass through and connected to the plasma actuator in one continuous piece. This allows for the insulation on the high voltage wire to remain intact from the high voltage transformer all the way to the plasma actuator. The pass through itself is made to fit the vacuum chamber from some scrap acrylic. Once the bolt hole pattern is drilled into the material a center hole is made such that the high voltage wire can fit through. A middle section of the insulation is cut away such that the bare wire sits inside of the center drilled hole. This is to allow separation between the inside of the chamber and out so that good vacuum can be sealed. This is also to help keep plasma from forming within the wire as well. The final step in construction is to use some JB Weld to seal the hole. This grey substance can be seen in Figure B. 1.

Figure B.1: The custom made high voltage pass-through used for high altitude testing.

Within the vacuum chamber it is necessary to take care of where the high voltage wire lays. As shown in Figure B.2 a suspension system of Kapton tape is used to keep the high voltage wire a sufficient distance from the vacuum chamber. If the wire is touching or in close proximity to the chamber walls arcing will occur creating undesired plasma formation. Also note in Figure B.2 the amount of Kapton tape used on the high voltage wire near the pass through area in the back of the chamber. Again, this is to prevent plasma formation between the wire and walls as this is the closest point to the chamber walls that the wire will be.

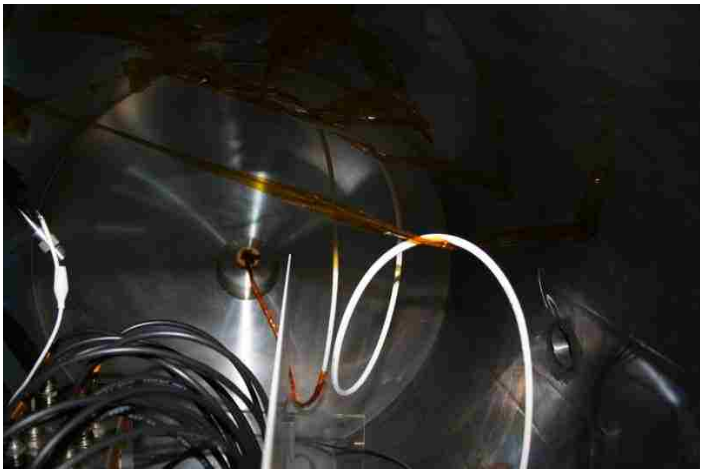

Figure B.2: Special care must be taken to insure that arcing does not occur between the high voltage wire and the vacuum chamber walls.

B.2. HIGH VOLTAGE TRANSFORMER CONSIDERATIONS

In order to prevent undesired operation of the plasma actuator a faraday cage must be built around the high voltage transformer used for this experiment. This is shown in Figure B.3 . The large leads on the transformer are capable of picking up ambient noise in the lab causing plasma to form on the actuator without the function generator operating. The faraday cage is able to shield out this noise which is approximately 16 kHz and most likely comes from the overhead lights. The high voltage probe is also placed inside of this faraday cage housing. Special care must be taken when running the high voltage wire out of the faraday cage to the vacuum chamber. This is due to the fact that the faraday cage must be grounded in order to function properly. If the high voltage wire is located too close to the grounded copper mesh arcing will occur. Kapton tapes as well as standoffs are used to further insulate and position the wire away from the grounded cage.

Figure B.3: The faraday cage is used to keep the high voltage transformer from picking up ambient noise.

B.3. GROUNDING SCHEMES AND BURIED ELECTRODE ATTACHEMENT

In this experiment it is especially important to keep track of all common grounds in order to prevent ground loops and unwanted electrical noise in the op-amp integrator circuit. The vacuum chamber itself is used as a low impedance grounding reference by attaching the ground wire from a three plug chord and plugging that chord into a wall socket. The faraday cage, op-amp circuit, and all V-dot probes are then connected to the chamber.

In order to keep the ground reference on both the plasma actuator and the op-amp integrator circuit with as low of an impedance as possible, standard coaxial cable is used to connect the ground. For the actuator in particular, coaxial cable connects all V-dot probes to a grounding box (shown in Figure B.4). Inside this grounding box all cables are connected together where a final coaxial cable then is connected to the chamber. The coaxial cable also serves the purpose of shielding out noise produced by adjacent V-dot probes. Without a shielded cable the signal that is read by the op-integrator circuit is noisier as well as larger in magnitude, both are adverse to the measurements trying to be made.

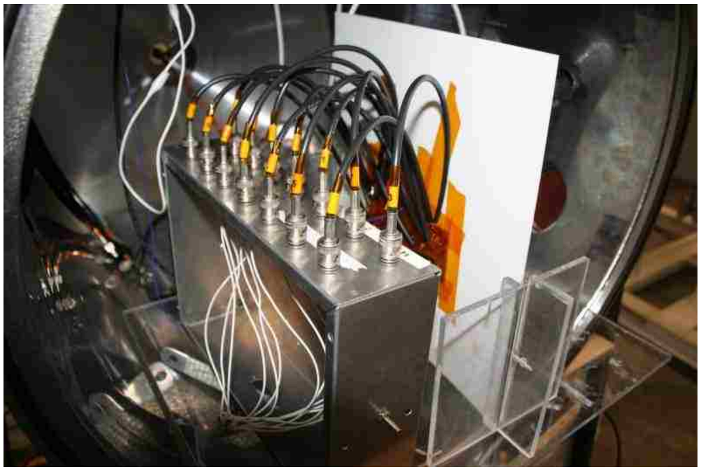

Figure B.4: Coaxial cable is used to ground each V-dot probe to a common point in a grounding box.

As an additional rule of thumb it is always good practice in this experiment to plug all electronics into the same power strip. In this case that would mean that the function generator, audio amplifier, and oscilloscope all need to be plugged into the same place. This helps to eliminate another possible ground loop.

In Figure B.4 it is also worthwhile to note the way the buried electrode is attached to the back of the Macor sheet. The V-dot probe array is laid flat against the Macor such that no air gap exists between it and the Macor. If there is an air gap not only can plasma form in this region, but the measurements of the surface potential from the V-dot probes will be inaccurate as well due to the fact that there is now a second dielectric to account for. Kapton tape is used to keep the buried electrode in the proper place.

B.4. ADDITIONAL OP-AMP INTEGRATOR COMMENTS

Shown in Figure B.5 is the actual op-amp integrator circuit used for this experiment. The op-amp is run off of four, nine volt batteries(two batteries wired together per side). Across the power inputs filter capacitors are used (small blue capacitors in Figure B.5) in order to keep noise from leaking into the high frequency signal that is being measured. To measure the output on the oscilloscope a simple Tektronix P2221 voltage probe is used in 1X mode. As a precaution against picking up the same 16 kHz noise that the transformer can pick up, a faraday cage was built around the circuit. This, however, improved the signal an immeasurable amount and is thus unnecessary.

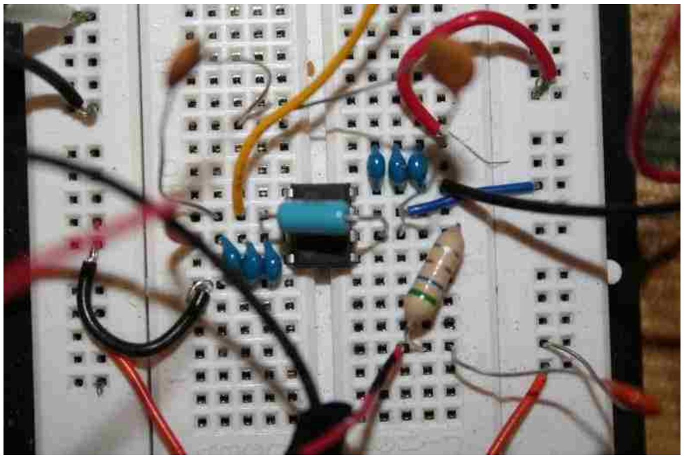

Figure B.5: The op-amp integrator circuit used in this experiment.

BIBLIOGRAPHY

1. C.L. Enloe, G.I.F., T.E. McLaughlin, Robert D. VanDyken, K.D. Kachner, Eric J. Jumper, and Thomas C. Corke, Mechanisms and Responses of a Single Dielectric Barrier Plasma Actuator: Plasma Morphology. AIAA Journal, 2004. 42(3): p. 6.

2. Moreau, E., Airflow control by non-thermal plasma actuators. Journal of Physics D: Applied Physics, 2007(40): p. 33.

3. Jerome Pons, E.M.a.G.T., Asymmetric surface dielectric barrier discharge in air at atmospheric pressure: electrical properties and induced airflow characteristics. Journal Of Physics D: Applied Physics, 2005. 38: p. 9.

4. Thomas C. Corke, C.L.E., and Stephen P. Wilkinson, Dielectric Barrier Discharge Plasma Actuators for Flow Control. Annual Review of Fluid Mechanics, 2009. 42: p. 27.

5. Corke, M.L.P.T.C., Separation control on high angle of attack airfoil using plasma actuators. AIAA Journal, 2004. 42: p. 8.

6. Corke, C.H.T.C., Plasma Flaps and Slats: An Application of Weakly Ionized Plasma Actuators. Journal of Aircraft, 2009. 46(3): p. 10.

7. Post, T.C.C.M.L., Overview of Plasma Flow Control: Concepts, Optimization, and Applications. 43rd AIAA Aerospace Sciences Meething and Exhibit, 2005: p. 15.

8. Mertz, T.C.C.B., Plasma Flow Control Optimized Airfoil. 44th AIAA Aerospace Sciences Meething and Exhibit, 2006: p. 13.

9. Mehul P. Patel, T.T.N., Srikanth Vasudevan, Plasma Actuators for Hingeless Aerodynamic Control of an Unmanned Air Vehicle. 3rd AIAA Flow Control Conference, 2008: p. 21.

10. Flint O. Thomas, T.C.C., Muhammad Iqbal, Alexey Kozlov, David Schatzman, Optimization of Dielectric Barrier Discharge Plasma Actuators for Active Aerodynamic Flow Control. AIAA Journal, 2009. 47(9): p. 10.

11. M. Forte, J.J., J. Pons, E. Moreau, G. Touchard, M. Cazalens, Optimization of a dieletric barrier discharge actuator by stationary and non-stationary measurements of the induced flow velocity: application to airflow control. Exp. Fluids, 2007. 43: p. 12.

12. J. Reece Roth, X.D., Optimization of the Aerodynamic Plasma Actuator as an Electrohydrodynamic (EHD) Electrical Device. 44th AIAA Aerospace Sciences Meething and Exhibit, 2008: p. 28.

13. Ryan Durscher, S.R., Novel Multi-Barrier Plasma Actuators for Increased Thrust. 48th AIAA Aerospace Scieneces Meeting and Exhibit Including the New Horizons Forum and Aerospace Exposition, 2010: p. 9.

14. James W. Gregory, C.L.E., Gabriel I. Font, and Thomas E. McLaughlin, Force Production Mechanisms of a Dielectric-Barrier Discharge Plasma Actuator, in 45th AIAA Aerospace Sciences Meeting and Exhibit, `, Editor. 2007, AIAA 2007-185: Reno, Nevada. p. 13.

15. V.M. Litvinov, V.V.S., and A.A. Uspenskii, Role of the Static Pressure in Experiments on Flow Control by Means of Surface Capacitor Discharges. Fluid Dynamics, 2006. 41(2): p. 6.

16. N. Benard, N.B., and E. Moreau, Electric Wind Produced by a Single Dielectric Barrier Discharge Actuator Operating in Atmospheric Flight Conditions - Pressure Outcome. 39th Plasmadynamics and Lasers Conference, 2008: p. 16.

17. N. Benard, N.B.a.E.M., Electric wind produced by a surface dielectric barrier dishcarge operating in air at different pressures: aeronautical control insights. Journal of Physics D: Applied Physics 2008. 41: p. 5.

18. Yun Wu, Y.L., Min Jia, Huimin Song, Zhigang Guo, Ximing Zhu, and Yikang Pu, Influence of operating pressure on surface dielectric barrier discharge plasma aerodynamic actuation characteristics. Applied Physics Letters, 2008. 93: p. 3.

19. Takashi Abe, Y.T., Shunichi Sato, and Nobara Kimura, Experimental Study for Momentum Transfer in a Dielectric Barrier Discharge Plasma Acutator. AIAA Journal, 2008. 46(9): p. 9.

20. N. Benard, E.M., Effects of Altitude on the Electromechanical Characteristics of a Single Dielectric Barrier Discharge Plasma Actuator. 41st Plasmadynamics and Lasers Conference, 2010: p. 17.

21. Philippe Versailles, V.G.-G., and Huu Duc Vo, Impact of Pressure and Temperature on the Performance of Plasma Actuators. AIAA, 2010. 48(4): p. 5.

22. C.L. Enloe, M.G.M., and T.E. McLaughlin, Time-correlated force production measurements of the dielectric discharge plasma aerodynamic actuator. Journal of Applied Physics, 2008. 103(073302): p. 7.

23. C.L. Enloe, T.E.M., J.W. Gregory, R.A. Medina, and W.S. Miller, Surface Potential and Electric Field Structure in the Aerodynamic Plasma Acutator, in 46th AIAA Aerospace Sciences Meeting and Exhibit. 2008, AIAA 2008-1103: Reno, Nevada. p. 11.

24. C.L. Enloe, G.I.F., T.E. McLaughlin, and D.M. Orlov Surface Potential and Longitudinal Electric Field Measurements in the Aerodynamic Plasma Actuator. AIAA Journal, 2008. 46(11): p. 11.

25. G.I. Font, C.L.E., T.E. McLaughlin, and D. Orlov, Plasma Discharge Characteristics and Experimentally Determined Boundary Conditions for a Plasma Actuator, in 45th AIAA Aerospace Sciences Meeting. 2007, AIAA 2007-0188: Reno, Nevada. p. 14.

26. Dmitry F. Opaits, G.N., Sohail H. Zaidi, Mikhail N. Schneider, Richard B. Miles, Alexandre V. Likhanskii, Sergey O. Macheret, DBD Plasma Actuators Driven by a Combination of Low Frequency Bias Voltage and Nanosecond Pulses. 48th AIAA Aerospace Scieneces Meeting and Exhibit, 2008(AIAA 2008-1372): p. 18.

27. T.G. Nichols, J.L.R., Fundamental Processes of DBD Plasma Actuators Operating at High Altitude. 50th Annual AIAA Aerospace Sciences Meeting, 2012: p. 23.

VITA

Timothy Nichols was born in Covington, Tennessee to Tina and Sam Nichols. He graduated 1st in his class from Greenbrier High School in May 2006 after which he pursued at Physics degree at Hendrix College in Conway, AR. Upon completion of his undergraduate degree he attended the Missouri University of Science and Technology to obtain a Master's degree in Aerospace Engineering. Throughout his academic career, Timothy has been a member of numerous academic honor societies and organizations including: the Society of Physics Students, Pi Mu Epsilon, and AIAA.

When not pursuing academic interests, Timothy gets out and enjoys nature as much as possible. He goes rock climbing, hiking, canoeing, and camping any chance he gets. He is also very interested in playing numerous different sports (basketball, baseball, soccer, racquetball, etc.) and living an overall healthy and active lifestyle.